minerals

Article

Zircon U–Pb Age and Geochemistry of Ore-Hosting Rocks from the Liuhe Orefield of the Jiapigou Gold Ore Belt, NE China: Magmatism and Tectonic Implications

Jian Zhang [1,2], Yanchen Yang [1,*], Piyi Guo [3] and Wukeyila Wutiepu [4]

1 College of Earth Sciences, Jilin University, Changchun 130061, China
2 Team 607, Jilin Nonferrous Metal Geological Exploration Bureau, Jilin 132000, China
3 Team 608, Jilin Nonferrous Metal Geological Exploration Bureau, Changchun 130000, China
4 Xinjiang Research Centre for Mineral Resources, Xinjiang Institute of Ecology and Geography, Chinese Academy of Sciences, Urumqi 830011, China
* Correspondence: yyc@jlu.edu.cn; Tel.: +86-431-88502128

Abstract: Liuhe gold orefield is being newly explored in the southeast part of the Jiapigou gold ore belt, and occurs in the Neoarchean basement composed of trondhjemite–tonalite–granodiorite (TTG). Zircon U–Pb data suggest that the ore-hosting magma emplacement in the Liuhe orefield mainly took place in two epochs: late Neoarchean to early Paleoproterozoic (ca. 2500 Ma) and early Jurassic of the Mesozoic era (ca. 170 Ma). The TTG rocks show higher $A1_2O_3$ (12.58 to 15.71%) and Na_2O/K_2O ratios (1.16 to 2.9), and lower MgO (0.93 to 2.73%) and Mg# values, with positive Eu anomaly and low Y and Yb content, and high Sr/Y (22.3–79.6), and the plot in the adakite field in the Sr/Y-Y discriminant diagram belongs to the modern island-arc adakite rocks. Samples in this study are plotted in the pre-plate collision area in the R1-R2 discrimination diagram, and fall into the VAG and VAG + Syn-COLG field in the Rb-Y + Nb and Nb-Y diagram, respectively, indicating that the magmatism is related to plate subduction. The ore-bearing TTGs of the late Neoarchean to early Paleoproterozoic deposits were derived from the partial melting of mafic lower crustal caused by the underplating of basaltic magma on the island-arc or active continental margin before plate collision. The magmatism of the Dajiagou deposit occurred in active continental margin setting associated with the westward subduction of the paleo-Pacific plate beneath Eurasian Plate during the early Jurassic of Mesozoic period.

Keywords: Liuhe orefield; TTG; Zircon U–Pb; major and trace element; adakite

Citation: Zhang, J.; Yang, Y.; Guo, P.; Wutiepu, W. Zircon U–Pb Age and Geochemistry of Ore-Hosting Rocks from the Liuhe Orefield of the Jiapigou Gold Ore Belt, NE China: Magmatism and Tectonic Implications. *Minerals* **2022**, *12*, 1121. https://doi.org/10.3390/min12091121

Academic Editor: Ryan Mathur

Received: 17 August 2022
Accepted: 1 September 2022
Published: 2 September 2022

1. Introduction

As the oldest and largest craton in China, the North China Craton (NCC) has been the subject of extensive research and attention owing to its complex evolution and abundant mineral resources [1–8]. The gold deposits are distributed along the margin of the NCC and generally occur in the Precambrian basement rocks or Phanerozoic felsic plutons [3,9–11]. From Jiaodong, many gold concentration areas lie along the margin of the NCC in a counterclockwise direction, including the Eastern Liaoning, Jiapigou, Chifeng–Chaoyang, Eastern Hebei, Zhan–Xuan, Daqingshan, Xiaoqinling–Xiongershan, and Western Qinling areas. The gold reserves in the NCC account for over 70% of all reserves in China [9,12]. As the gold mining area with the longest mining history in China, the northern margin of the NCC is rich in gold resources, with more than 900 t of Au. The most famous is the Jiapigou gold mining area, which has a mining history of nearly 200 years and has produced 150 t of gold, includes dozens of gold deposits such as the Erdaogou, Xiaobeigou, Banmiaozi, and Bajiazi deposits [4,13,14]. It is regarded as one of the most important gold-producing districts in China [4,15].

The Jiapigou gold ore belt is located in the eastern part of the northern margin of the NCC, with the Siberian plate and the Yangtze Craton to the north and south, respectively, and the Pacific plate to the east (Figure 1a,b) [16]. The entire gold belt is located in the NW Jiapigou fault between the NE Liangjiang fault and the Huifahe fault [5]. It lies in the Neoarchean basement and is mainly composed of gray gneisses, including Neoarchean–Paleoproterozoic trondhjemite–tonalite–granodiorite (TTG). However, it was extensively reworked by the closure of the Paleo-Asian Ocean between the NCC and the Siberian plate and the subduction of the Pacific plate beneath the East Asian continent in the Mesozoic. The Jiapigou fault suffered from ductile shear in the early stage and brittle deformation in the late stage; the ore bodies lie in the ductile–brittle shear zone and are obviously controlled by structure [14,17–21]. Although the Jiapigou gold ore belt contains several large gold ore fields, such as the Jiapigou, Banmiaozi, and Haigou gold ore fields, the shallow resources have been exhausted by the long mining history. The Liuhe gold ore field is a newly prospected ore field located southeast of the Jiapigou gold ore belt. It includes the large Dajiagou deposit, and the small-scale Zhemagou, Gaoligou, and Binghugou deposits. According to the traditional Archean gold metallogenic theory, the large gold deposits generally occur in the granite-greenstone belt, such as Canada, Australia, and South Africa, while there are a few reports of large gold deposits in high-grade metamorphic zones. The ore morphology, ore type and other characteristics of the deposit in the Liuhe orefield are not very different from those of gold deposit in the Jiapigou granite-greenstone belt, which makes it necessary to further discuss the relationship between high-intensity metamorphic zone and gold mineralization. Since the discovery of the Liuhe gold deposit in the 1990s, it has been a hot spot for geologists; however, because of the late exploration and development in this area, the lack of research on deposit geology and genesis has seriously limited understanding of the metallogenic regularity in this area and restrained future exploration. In this paper, we report new geological, petrological, zircon U–Pb and whole-rock geochemical data for the Djiagou, Daxigou, Binghugou, Gaoligou, and Zhemagou deposits, combined with the latest data of the Liuhe ore field and Jiapigou gold ore belt, and the petrogenesis of ore-bearing rocks, the metallogenic geodynamic setting, genesis, and metallogenic model of these deposits are expounded in detail.

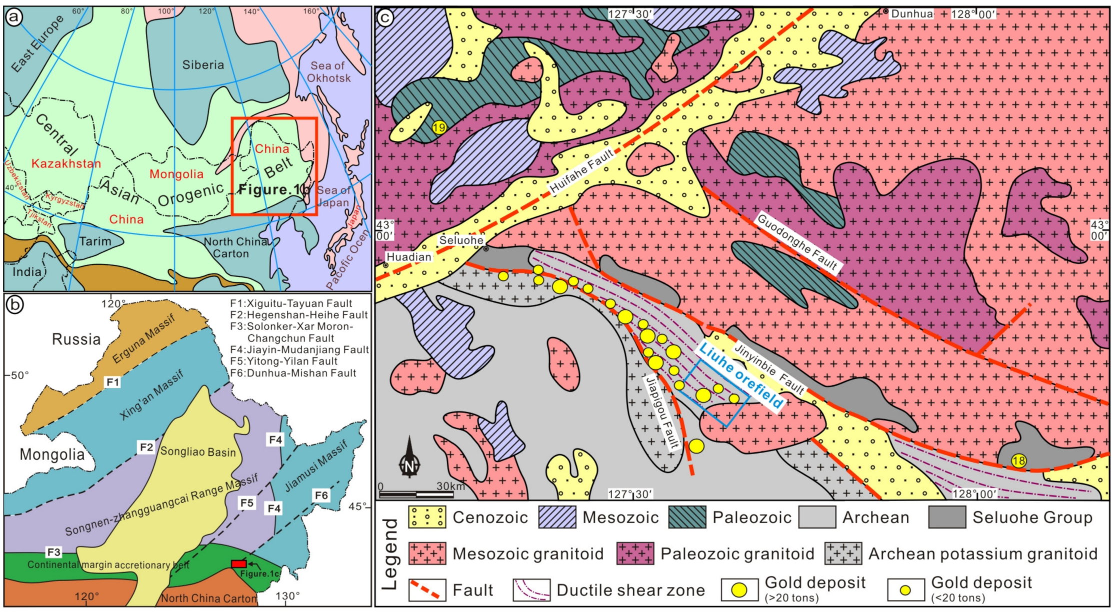

Figure 1. (**a**) General map showing the location of NE China, modified after Safonova and Santosh (2014) [22]; (**b**) tectonic sketch map of NE China (modified after Wu et al., 2011) [23]; (**c**) regional geological map of the Jiapigou gold ore belt, NE China. Showing the distribution of the major gold deposits (modified after Zeng et al., 2017) [24].

2. Regional Geology

The Liuhe area is located in the northern end of the Longgang continental nucleus in the eastern part of the northern NCC, and on the platform marginal active belt at the junction of the NCC and Jihei fold belt. It belongs to the same tectonic unit as the Jiapigou gold ore field, which is the southeast extension of the Jiapigou gold belt [25,26] (Figure 1c). The Liuhe area is an Archean high-grade metamorphic terrain, dominated by Archean rock units. Owing to the influence of the regional metamorphism and tectonic movement, the rock metamorphism and deformation are extremely intense [27]. The exposed rocks are mainly gray gneiss (TTG), including Wutai potassium and sodium granites, the supercrust rocks and Fuping felsic gneiss are mostly "floating" in the gray gneiss, while the metamorphic intermediate–basic intrusive rocks mostly occur as dikes (Figure 2) [28,29]. The magmatic activities in the Liuhe area were relatively frequent and can be traced back to the Archean. The Archean–Proterozoic magmatic rocks have undergone multiple metamorphism and deformation and mostly became gray gneisses [13,24]. With the intensification of crustal activity and diapirism, Caledonian granodiorite intruded in a large area along the margin of the platform. Under the influence of the Indosinian movement, the intermediate–basic to acidic magma of the Wudaoliuhe sequence emplaced and was represented by the EW trending Wudaoliuhe granite [30]. In the Yanshanian period, quartz porphyry, granite porphyry, and rhyolitic porphyry sporadically distributed in the area. Mesozoic intermediate–basic, acidic, and alkaline dikes distributed along the NE-trending tectono-magmatic activity zone between the Toudaoliuhe–Wudaoliuhe sequence, among which cryptoexplosive breccia bodies were found in Jiancaogou and Binghugou in Sandaoliuhe [31]. In the Himalayan period, basalt was ejected near the upper and lower walls of the NE-trending structure of the Erdaosonghua River. Magmatic rocks from the Archean to the Mesozoic Jurassic were developed in the study area, including Neoarchean granitic gneiss, Proterozoic intrusive rocks, and Mesozoic intrusive rocks and volcanic rocks. The Neoarchean granitic gneisses are gneissic and contain a large number of supracrustal xenoliths. The Proterozoic intrusive rocks are the products of Archaean craton activation, and are mainly weakly gneissic granitic gneiss. The Paleozoic magmatism was not developed. Mesozoic intrusive rocks are mainly granitic complexes, which occur as irregular intrusives or composite complexes. Archean granites are widely outcropped in the study area, mainly including TTG series and monzogranitic and potassium granitic gneiss. The TTG assemblage is trondhjemite–tonalite–granodiorite, which is largely outcropped on the west side of the Jiapigou ductile shear zone. Monzogranitic and potassium granitic gneiss are widely exposed in the east of the study area, mainly distributed along the ductile shear zone in a zonal pattern. Due to the influence of regional metamorphism and the transformation of tectonic deformation, the contact relationship between them is not clear or covered up, and the intrusion of light metagranite into potassic granitic gneiss can be seen in some areas. In general, Archean granites evolved from sodic to potassic.

The Liuhe area is located in the active belt along the margin of the NCC, with developed fault structures. The main structure is the NW-trending ductile–brittle shear zone, which is the southeast extension of the NW-trending ore-controlling structure of the Jiapigou gold ore field, and they are distributed parallel to each other in the outer contact zone of the west side of the Mesozoic Wudaoliuhe monzogranite [32]. The early stage has the characteristics of a ductile shear zone, and the late stage has the characteristics of a brittle fracture structure. In the ductile–brittle shear zone, dikes, porphyry, and cryptoexplosive breccia in different periods can be seen, indicating that the ductile–brittle shear zone has the characteristics of multiple structural superposition and multi-stage dike intrusion and is also the main ore-controlling structure in the Liuhe area [33]. The ductile shear zone cuts through the basement rock–gray gneiss (TTG), proving that the latest formation time of the shear zone was late Archean–Early Proterozoic.

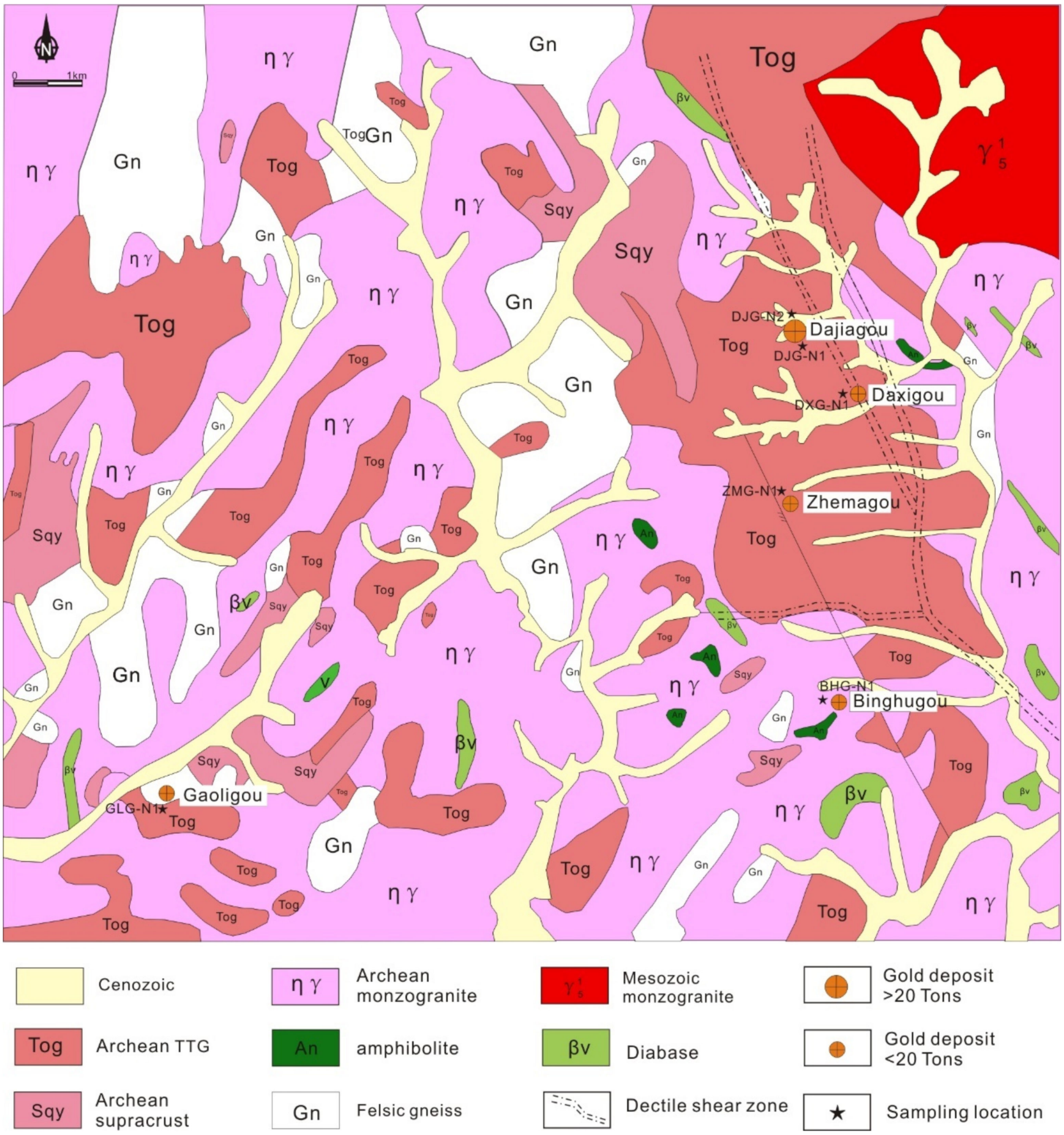

Figure 2. Simplified geological map of the Liuhe gold orefield, NE China.

3. Samples and Analytical Methods

3.1. Samples and Petrography

Among the 6 samples collected in this study, 5 were Neoarchean TTG rocks and 1 was Mesozoic intrusive rock. Detailed descriptions of the rock samples and their lithofacies are given below and shown in Table 1.

Monzogranite (sample DJG–N1): light fleshy red in color, of a medium grain and massive structure. It was composed of fleshy red potash feldspar (35–40%), gray plagioclase (30%), quartz (25%) and so on; the plagioclase was partially altered into kaolin and sericite, the quartz particle size was 0.2–3 mm, and most were anhedral granular crystals filled in feldspar minerals; a small amount of pyrite and other metal minerals were seen locally (Figure 3a).

Table 1. Simplified locations and petrological characteristics for the samples from the Liuhe orefield, NE China.

Sample No.	Lithology	Location	Texture/Structure	Mineral Assemblage
BHG-N1	Monzogranitic breccia	Binghugou gold deposit	brecciform structure	Kfs(35%) + Pl(30%) + Qz(25%) + Bi(5%)
DJG-N1	Monzogranite	Dajiagou gold deposit	medium-grain texture, massive structure	Kfs(35%) + Pl(30%) + Qz(25%) + Bi(5%)
DJG-N2	Diorite	Dajiagou gold deposit	fine-grained texture, massive, veined structure	Pl(50%) + Hb(35%) + Kfs(10%) + Qz(5%)
DXG-N1	Monzogranite	Daxigou gold deposit	medium-grain texture, massive structure	Kfs (40%) + Pl(30%) + Qz(25%)
GLG-N1	Monzogranite	Gaoligou gold deposit	medium-grain texture, gneissic structure	Kfs(35%) + Pl(25%) + Qz(25%) + Bi(10%)
ZMG-N1	Trondhjemite	Zhemagou gold deposit	medium-grain texture, massive structure	Pl(50%) + Qz(35%)+ Bi(10%)

Note. Kfs: K-feldspar; Pl: plagioclase; Qz: quartz; Bi: biotite; Hb: hornblende.

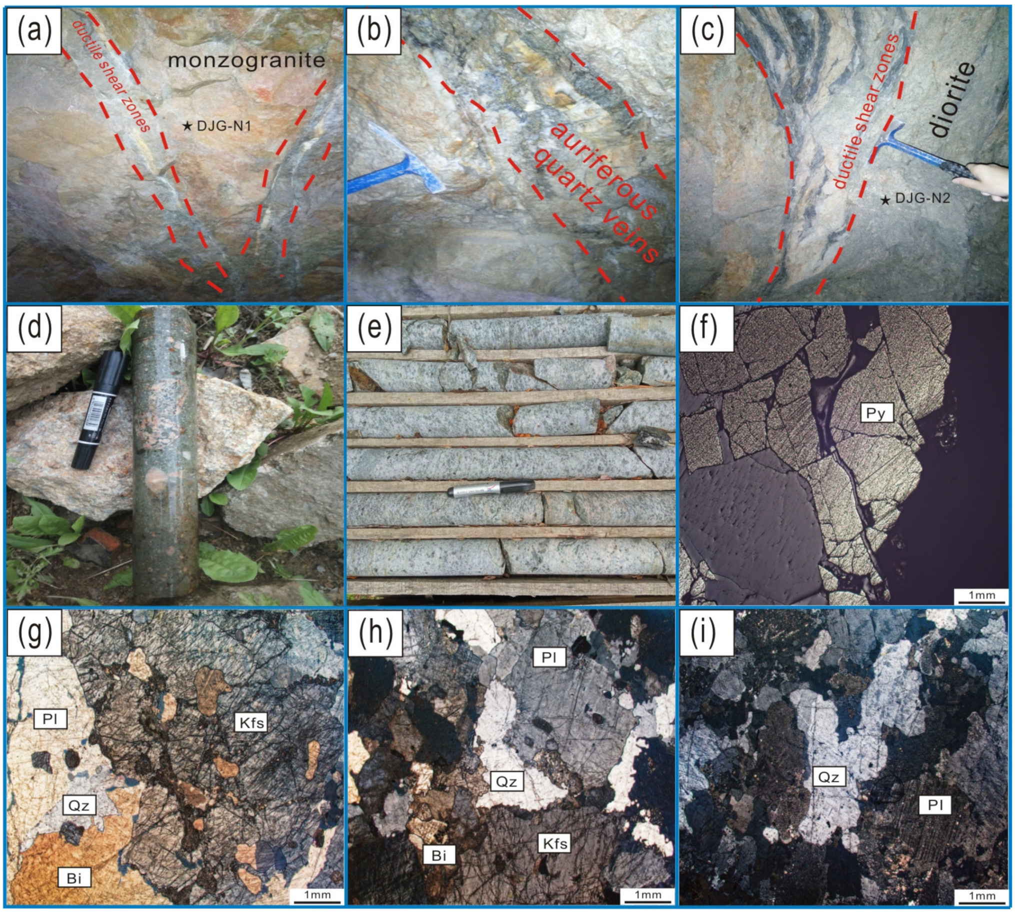

Figure 3. Representative outcrop and photomicrographs (cross-polarized light) for representative igneous rocks in the Liuhe gold Orefield, NE China: (**a**) spatial relationship between monzogranite and ductile shear zones; (**b**) auriferous quartz veins in the ductile shear zones; (**c**) spatial relationship between ductile shear zones and altered fine-grained diorite; (**d**) monzogranitic breccia (BHG-N1); (**e**) trondhjemite (ZMG-N1); (**f**) pyrite in diorite (DJG-N2); (**g**) photomicrograph of monzogranite (GLG-N1); (**h**) photomicrograph of monzogranitic breccia (BHG-N1); (**i**) photomicrograph of trondhjemite (ZMG-N1). Pl: plagioclase; Kfs: Kfeldspar; Qz: quartz; Bi: biotite; Ser: Sericite Py: pyrite.

Diorite (sample DJG–N2): the rock was gray-black, of a fine-grained, massive, vein-like structure. Among them, the size of the plagioclase was 0.1–0.3 mm, the content was 40–50%; sericite alteration occurred mostly, hornblende was altered into chlorite, and the content was 30%; pyrite was a cubic crystal with a particle size of 0.0n mm, some crystals reached 0.5 mm, and the content was ±1–10%. When the rocks were subjected to strong tectonic forces and alteration, discoloration occurred and diorite mylonites were found (Figure 3b,c,f).

Monzogranitic breccia (sample BHG–N1): the rock was reddish-brown and brecciform in structure. The breccia was monzogranite with a subangular shape, the cementation was mainly crystal and rock powder of monzogranitic rocks, and the cementation was mainly pore type; contact cementation was also seen locally (Figure 3d,h).

Trondhjemite (sample ZMG–N1): the rocks were mainly grayish white, partially light fleshy red, medium granular texture, massive structure. Main mineral composition: plagioclase was columnar, particle size 0.4–2.0 mm, partially altered into sericite, common polysynthetic twinning, content 50%; quartz was anhedral granular, particle size 0.1–2.0 mm, content 35%; biotite was flake, particle size 0.2–2.5 mm, content 10%, mostly altered into chlorite and magnetite; potash feldspathization was seen locally in the rocks (Figure 3e,i).

Monzogranite (sample GLG–N1): gray-red, medium granular texture, gneissic structure, particle size 3–4 mm. The main mineral components included potassium feldspar, which was columnar, partially altered into kaolin, content 35%; plagioclase was irregular tabular, and there was polysynthetic twinning, some of them were altered into kaolin and sericite, and the content was 25%; quartz was anhedral granular, content of 25%; biotite was flake and varied in size among felsic minerals, with a content of 10% (Figure 3g).

Monzogranite (sample DXG–N1): the rock was light fleshy red, medium-coarse granular texture, massive structure. Orthoclase was anhedral crystal, with a content of about 35%; plagioclase was irregular granular, common sericite, local visible residual polysynthetic twinning, content was about 30%; potassium feldspar was irregular anhedral crystal, content was about 5%; quartz was anhedral granular, content was about 25%; a small amount of biotite and other minerals were detected.

3.2. Whole-Rock Major and Trace Element Analysis

Major elements, trace elements, and rare earth elements (REEs) were analyzed and tested in the ALS Chemex, Guangzhou, China. The major elements were tested by X–ray fluorescence spectrometry (XRF), and the FeO was analyzed by the volumetric method of hydrofluoric acid–sulfuric acid solution and potassium dichromate titration. The analysis accuracy was better than 2%. Trace and rare earth elements were determined using inductively coupled plasma mass spectrometry (ICP-MS). The analysis process was as follows: weigh the 0.0500 g sample in the Teflon high-pressure inner tank, add 1 mL HF and 0.5 mL HNO_3, cover the Teflon lid, seal it in the steel sleeve, and place it in the oven at 190 °C for 48 h. After cooling, remove the inner tank and evaporate on the electric heating plate until nearly dry. Add 0.5 mL HNO_3 and steam until nearly dry, repeat twice; add 5 mL (1 + 1) HNO_3, reseal in the steel jacket, and maintain at 130 °C for 3 h. After cooling, move the sample into a clean plastic bottle with a constant volume of 50 mL. The computer test analysis accuracy was better than 5%.

3.3. Zircon U–Pb Isotopic Analyses

The zircon U–Pb (LA–ICP–MS) method was used to date the main rocks in the samples from the study area. The zircon samples were selected by traditional gravity and magnetic separation methods in the laboratory of the Hebei Institute of Regional Geology and Mineral Resources Survey, Langfang, China. Laser ablation (LA)–ICP–MS zircon U–Pb geochronology from 14 samples was carried out at the MLR Key Laboratory of Mineral Resources Evaluation in Northeast Asia, Jilin University, Changchun, China. A Coherent COMPEx Pro ArF excimer laser was used for laser ablation. The mass spectrometry was performed with an Agilent 7500 A quadrupole plasma mass spectrometer [34]. The standard zircon 91500 (1062 Ma) was used as the external standard for isotope ratio correction [35], the standard zircon GJ–1 was used as the blind sample for monitoring, the international standard sample NIST610 was used as the external standard for element content, and Si was used as the internal standard element for calculation. Isotope ratio and element content were calculated using GLITTER software [36]. Isoplot calculates Concordia ages and images were given using Isoplot/Ex (3.0) [37]. Common Pb correction was calculated using the program presented by Anderson (2002) [38].

4. Analytical Results

4.1. Major and Trace Element Geochemistry

Among the 22 samples analyzed, except DJG–N2–Q1 to DJG–N2–Q4 from the Dajiagou deposit, which are altered fine-grained diorite, 18 samples, including trondhjemite and monzogranite, are Neoarchean metamorphic plutonic rocks, i.e., TTG rocks. The whole-rock geochemical data and relevant parameters of the samples are listed in Table 2, and the detailed characteristics are described as below:

(1) TTG

The chemical analyses of the 18 Neoarchean samples show high SiO_2 (60.51–72.38%) and Na_2O ((2.95–4.62%), low K_2O (1.72–3.32%), MgO (0.93–2.37%), TiO_2 (0.22–0.55%), and TFe_2O_3 (2.30–5.53%), and variable CaO (1.72–7.07%) and Al_2O_3 (11.42–16.66%), with K_2O/Na_2O ratios of 0.37–0.94, and Mg# values of 0.34–0.54 (Table 2). Rare earth elements (REEs) for the TTG samples showed a wide range of ΣREE values (55.02–283.11 ppm), light rare earth element (LREE) values from 51.01 to 277.79 ppm, rare earth element (HREE) values from 4.01 to 10.01 ppm, LREE/HREE ratios from 10.73 to 52.22, and $(La/Yb)_N$ values from 16.85 to 97.34. The chondrite–normalized REE patterns showed relative enrichment in LREEs, depletion in HREEs, and slightly positive Eu anomalies (Figure 4a). Plotting the data for these TTG samples on primitive mantle normalized spider diagrams indicated that they were enriched in large ion lithophile elements (LILEs; e.g., Rb, Ba, Th, and K) and depleted in high field strength elements (HFSEs; e.g., Ti, Nb, and Ti). Sr was mostly negative anomalies of varying degrees, and a few samples had no or very slightly positive Sr anomalies, indicating the existence of crystallization differentiation of plagioclase and biotite and local enrichment of plagioclase during the magmatic evolution (Figure 4b).

Table 2. Whole-rock major (wt.%) and trace element (ppm) compositions of TTG gneisses and diorites from the deposits in the Liuhe orefield.

Sample	GLG-N1-Q1	GLG-N1-Q2	GLG-N1-Q3	GLG-N1-Q4	DJ-N1-Q1	DJ-N1-Q2	DJ-N1-Q3	DJ-N2-Q1	DJ-N2-Q2	DJ-N2-Q3	DJ-N2-Q4
SiO_2	65.29	67.27	61.66	67.08	65.88	63.92	63.70	42.53	43.92	44.17	40.91
Al_2O_3	16.28	15.46	16.66	16.07	15.26	15.91	15.13	11.72	10.29	10.89	10.87
Fe_2O_3T	4.20	4.91	5.41	3.68	4.67	4.74	5.09	15.88	15.88	15.60	16.94
CaO	3.58	3.37	4.45	3.58	6.11	7.07	5.46	7.24	8.66	8.38	7.47
MgO	2.04	1.28	2.73	1.77	2.14	2.57	2.06	12.70	12.55	11.75	13.55
K_2O	1.87	1.88	1.91	1.72	1.74	1.79	2.35	3.28	1.81	2.77	1.86
Na_2O	4.55	4.15	4.52	4.62	4.30	3.31	3.36	0.35	0.27	0.36	0.38
MnO	0.06	0.05	0.10	0.05	0.12	0.12	0.10	0.20	0.22	0.28	0.22
TiO_2	0.44	0.46	0.38	0.40	0.50	0.47	0.55	2.19	1.86	2.03	2.68
P_2O_5	0.18	0.15	0.26	0.16	0.08	0.11	0.09	0.20	0.18	0.16	0.23
LOI	1.53	0.78	1.69	1.31	0.69	1.04	1.48	1.17	1.89	1.14	1.81
Rb	117.5	74.4	110.0	104.5	80.6	86.7	107.0	115.3	70.9	113.5	61.0
Sr	337	350	358	335	221	238	298	210	133	131	193
Ba	262	788	250	248	101	83	142	550	175	258	309
V	32	67	36	27	91	95	136	369	337	357	448
Cr	70	41	69	67	252	223	274	1040	910	870	1020
Nb	15.8	8.6	12.2	14.4	4.7	4.7	4.2	12.7	12.1	10.0	14.0
Ta	0.82	0.59	0.50	0.69	0.20	0.30	0.29	0.83	0.95	0.81	1.10
Zr	336	202	205	291	95	98	105	163	153	135	174
Hf	8.3	4.9	4.8	7.2	2.2	2.4	2.6	4.2	4.5	3.9	5.2
Th	2.92	12.10	2.60	2.58	2.18	4.70	7.78	2.45	2.24	1.99	2.58
U	1.45	0.67	0.74	1.42	0.30	0.32	0.64	0.45	0.42	0.27	0.39
Pb	11.2	15.2	11.5	12.8	2670	106.5	140.0	82.6	96.1	29.9	43.6
Co	11.3	11.0	13.3	11.1	21.9	17.6	21.1	88.8	80.8	69.6	114.0
Zn	80	83	95	64	312	118	188	256	252	173	298
Sn	1.0	1.6	1.0	1.1	1.2	1.2	1.1	1.9	2.1	1.4	1.4
Ni	34.3	11.9	38.3	35.2	96.5	103.5	121.5	440.0	461.0	375.0	535.0
Li	11.3	6.4	10.4	10.1	12.3	7.8	8.6	63.2	23.9	21.4	70.4
Mo	1.64	1.73	1.01	1.51	2.23	2.54	1.97	0.85	0.81	0.85	1.11
La	26.1	38.5	32.8	25.5	15.5	20.6	23.4	18.0	16.3	14.4	19.2
Ce	47.8	70.9	65.6	46.1	29.2	38.2	45.1	42.8	35.7	32.6	43.5
Pr	5.03	7.64	7.53	4.83	3.37	4.34	5.20	5.97	5.10	4.51	5.99
Nd	17.3	26.0	27.2	16.6	12.9	16.0	19.3	26.1	23.3	20.1	26.1
Sm	2.48	4.03	4.51	2.07	2.45	2.97	3.46	6.26	5.93	5.07	6.24
Eu	0.93	1.11	1.11	0.96	0.84	1.15	0.81	1.86	2.01	1.58	1.81
Gd	1.74	2.84	3.38	1.69	2.19	2.48	2.66	6.00	6.23	5.10	6.20
Tb	0.22	0.33	0.39	0.21	0.32	0.34	0.36	0.87	0.97	0.77	0.90
Dy	1.10	1.75	2.16	1.07	1.62	1.90	1.97	4.71	5.31	4.69	5.02
Ho	0.22	0.31	0.42	0.22	0.30	0.35	0.35	0.85	0.96	0.86	0.87
Er	0.67	0.80	1.17	0.59	0.76	0.87	0.97	2.22	2.35	2.10	2.44
Tm	0.10	0.12	0.17	0.09	0.10	0.11	0.14	0.30	0.32	0.28	0.31

Table 2. *Cont.*

Sample	GLG-N1-Q1	GLG-N1-Q2	GLG-N1-Q3	GLG-N1-Q4	DJ-N1-Q1	DJ-N1-Q2	DJ-N1-Q3	DJ-N2-Q1	DJ-N2-Q2	DJ-N2-Q3	DJ-N2-Q4
Yb	0.74	0.73	1.13	0.61	0.62	0.63	0.83	1.79	1.85	1.68	1.85
Lu	0.12	0.10	0.18	0.10	0.08	0.09	0.13	0.24	0.28	0.24	0.27
Y	6.2	8.0	11.4	5.8	8.4	9.8	9.9	23.3	22.8	21.1	23.4
ΣREE	104.6	155.2	147.8	100.6	70.3	90.0	104.7	118.0	106.6	94.0	120.7
ΣLREE	99.6	148.2	138.8	96.1	64.3	83.3	97.3	101.0	88.3	78.3	102.8
ΣHREE	4.9	7.0	9.0	4.6	6.0	6.8	7.4	17.0	18.3	15.7	17.9
LREE:HREE	20.3	21.2	15.4	21.0	10.7	12.3	13.1	5.9	4.8	5.0	5.8
$(La:Sm)_N$	6.6	6.0	4.6	7.7	4.0	4.4	4.3	1.8	1.7	1.8	1.9
$(La:Yb)_N$	23.8	35.6	19.6	28.2	16.9	22.0	19.0	6.8	5.9	5.8	7.0
Mg#	0.49	0.34	0.50	0.49	0.48	0.52	0.45	0.62	0.61	0.60	0.62
δEu	1.3	1.0	0.8	1.5	1.1	1.3	0.8	0.9	1.0	0.9	0.9
δCe	0.9	0.9	1.0	0.9	0.9	0.9	0.9	1.0	0.9	1.0	1.0
Sample	**DXG-N1-Q1**	**DXG-N1-Q2**	**DXG-N1-Q3**	**DXG-N1-Q4**	**BHG-N1-Q1**	**BHG-N1-Q2**	**BHG-N1-Q3**	**BHG-N1-Q4**	**ZMG-N1-Q1**	**ZMG-N1-Q2**	**ZMG-N1-Q3**
SiO_2	65.90	60.51	62.23	62.04	72.17	70.36	70.78	72.38	63.33	65.30	63.42
Al_2O_3	14.36	13.48	11.42	13.80	14.58	14.16	14.88	14.22	14.88	14.94	15.38
Fe_2O_3T	4.30	5.45	4.43	5.01	2.30	3.55	2.48	2.39	5.03	4.31	5.53
CaO	1.77	4.09	5.32	3.47	2.10	1.93	2.21	1.72	3.17	2.88	2.95
MgO	1.62	2.38	2.56	2.11	0.98	1.26	1.20	0.93	2.13	1.62	2.15
K_2O	2.93	2.78	2.66	2.23	2.80	2.39	2.37	1.91	3.32	3.16	2.66
Na_2O	3.54	3.17	3.22	3.32	3.75	2.95	3.90	3.38	3.52	3.48	3.45
MnO	0.04	0.06	0.08	0.05	0.02	0.03	0.02	0.02	0.05	0.05	0.06
TiO_2	0.49	0.50	0.33	0.46	0.35	0.29	0.42	0.22	0.45	0.39	0.53
P_2O_5	0.10	0.11	0.09	0.10	0.09	0.11	0.09	0.07	0.17	0.16	0.27
LOI 1000	0.89	1.94	0.53	0.24	1.25	1.20	1.27	1.11	0.67	0.10	0.06
Rb	108.0	167.0	139.0	166.8	79.7	112.5	80.9	104.0	81.5	88.6	103.5
Sr	184	116	145	125	348	459	354	414	398	421	489
Ba	326	235	208	254	830	1360	671	1180	1065	1280	1205
V	89	89	54	80	34	46	33	28	72	65	63
Cr	80	89	51	86	40	57	40	42	98	80	87
Nb	5.3	5.7	3.3	5.2	3.6	2.7	4.3	2.1	6.1	6.0	9.5
Ta	0.49	0.50	0.31	0.39	0.23	0.20	0.20	0.05	0.40	0.40	0.64
Zr	251	236	157	226	139	186	89	138	167	173	106
Hf	7.0	6.6	4.3	6.2	4.2	5.2	2.6	3.8	4.9	4.8	3.1
Th	13.80	1.30	0.43	2.61	21.6	15.80	8.47	7.63	1.19	1.37	2.05
U	0.53	0.51	0.33	0.45	0.32	0.33	0.19	0.25	0.41	0.40	0.41
Pb	14.2	7.6	99.4	10.6	18.6	22.8	16.9	21.4	11.9	14.6	14.0
Co	18.0	13.8	9.0	13.3	6.5	7.4	7.6	6.0	15.4	10.7	13.6
Zn	57	66	62	63	36	42	44	33	71	59	75
Sn	0.6	0.6	0.6	0.6	1.1	1.1	1.1	1.0	1.0	0.9	1.0

Table 2. *Cont*.

Sample	DXG-N1-Q1	DXG-N1-Q2	DXG-N1-Q3	DXG-N1-Q4	BHG-N1-Q1	BHG-N1-Q2	BHG-N1-Q3	BHG-N1-Q4	ZMG-N1-Q1	ZMG-N1-Q2	ZMG-N1-Q3
Ni	32.6	37.4	27.3	38.5	18.3	15.7	23.8	12.2	29.5	21.6	29.4
Li	24.9	10.6	5.2	11.0	9.0	9.0	10.8	8.5	22.4	12.6	27.8
Mo	0.99	1.91	1.07	1.43	0.98	0.83	0.86	0.99	1.57	1.23	1.32
La	82.3	21.9	13.8	25.5	46.5	39.8	38.3	32.7	30.5	27.0	35.3
Ce	136.5	37.1	23.3	42.9	66.2	61.4	52.1	46.9	52.4	45.8	64.9
Pr	13.40	3.91	2.54	4.43	6.74	6.18	5.43	4.65	6.02	5.19	7.79
Nd	39.8	13.6	8.8	14.3	20.6	20.1	16.8	14.8	20.8	18.6	28.1
Sm	4.28	1.92	1.67	2.01	2.74	3.01	2.47	2.20	3.02	2.88	4.28
Eu	1.51	1.05	0.90	1.01	1.33	1.39	1.29	1.42	1.21	1.27	1.40
Gd	2.38	1.78	1.43	1.53	1.90	2.21	1.71	1.58	2.21	2.21	3.63
Tb	0.24	0.20	0.19	0.18	0.24	0.29	0.23	0.21	0.29	0.29	0.47
Dy	1.18	1.09	0.99	0.97	1.16	1.51	1.13	1.07	1.60	1.60	2.46
Ho	0.21	0.22	0.19	0.18	0.20	0.27	0.20	0.19	0.30	0.33	0.48
Er	0.55	0.63	0.53	0.51	0.53	0.66	0.49	0.49	0.86	0.98	1.33
Tm	0.08	0.09	0.08	0.08	0.07	0.10	0.07	0.07	0.13	0.15	0.20
Yb	0.57	0.61	0.51	0.57	0.42	0.63	0.42	0.41	0.91	0.93	1.25
Lu	0.11	0.11	0.09	0.10	0.07	0.10	0.07	0.07	0.16	0.15	0.19
Y	5.2	5.2	5.3	4.9	5.1	7.2	4.9	5.2	8.6	8.4	13.0
ΣREE	283.1	84.2	55.0	94.3	148.7	137.7	120.7	106.8	120.4	107.4	151.8
ΣLREE	277.8	79.5	51.0	90.2	144.1	131.9	116.4	102.7	114.0	100.7	141.8
ΣHREE	5.3	4.7	4.0	4.1	4.6	5.8	4.3	4.1	6.5	6.6	10.0
LREE:HREE	52.2	16.8	12.7	21.9	31.4	22.9	26.9	25.1	17.6	15.2	14.2
$(La:Sm)_N$	12.1	7.2	5.2	8.0	10.7	8.3	9.8	9.3	6.4	5.9	5.2
$(La:Yb)_N$	97.3	24.2	18.2	30.2	74.6	42.6	61.5	53.8	22.6	19.6	19.0
Mg#	0.43	0.47	0.54	0.46	0.46	0.42	0.49	0.44	0.46	0.43	0.44
δEu	1.3	1.7	1.7	1.7	1.7	1.6	1.8	2.2	1.4	1.5	1.1
δCe	0.9	0.9	0.9	0.9	0.8	0.8	0.8	0.8	0.9	0.9	0.9

Note: LOI = loss on ignition. Mg# = 100 × molar $Mg^{2+}/(Mg^{2+} + Fe^{2+})$. TFeO = FeO + 0.8998 × Fe_2O_3. A/CNK = molar $Al_2O_3/(CaO + Na_2O + K_2O)$; letter N in footnote means normalization to chondrite, and the value referred to Sun and Mcdonough (1989) [39].

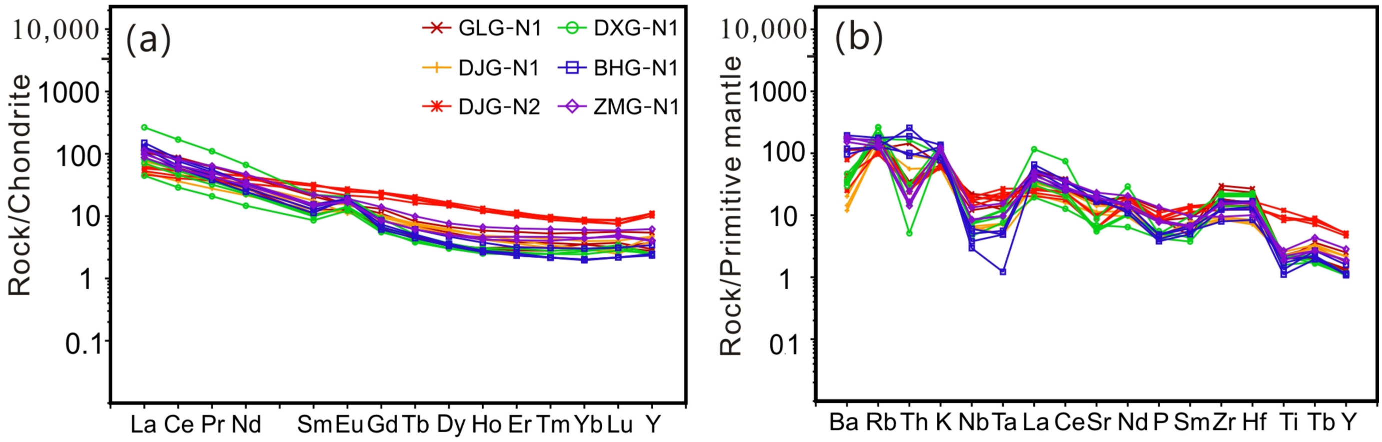

Figure 4. Chondrite-normalized REE pattern (**a**) and primitive mantle (PM) normalized spider diagram (**b**) for the TTG gneisses and diorites in the Liuhe deposits. Primitive mantle and chondrite values are from McDonough and Sun (1995) [40] and Sun and McDonough (1989) [39], respectively.

(2) Fine-grained diorite

The four fine-grained samples showed low SiO_2 (40.91–44.17%) and Na_2O (0.27–0.38%) contents, and intermediate K_2O (1.81–3.28%), Al_2O_3 (10.29–11.72%), CaO (7.24–8.66%), and TFe_2O_3 (15.60–16.94%) contents, and had relatively high K_2O/Na_2O ratios of 4.89–9.37 and Mg# value (0.60–0.62) (Table 2). The analysis results of trace and rare earth elements indicated that the diorite had a relatively high content of REEs (93.98–120.70 ppm), relatively enriched LREEs, depleted HREEs ($\sum LREE/\sum HREE$ = 4.84–5.95, $(La/Yb)_N$ = 5.78–7.00), and the fractionation between the LREEs and HREEs was not obvious; δEu was 0.88–1.00, there was no Eu anomaly (Figure 4a). The diorite was relatively enriched in Rb (61.0–115.3 ppm), Ba (175–550 ppm), K (14,000–25,800 ppm) and other large ion lithophile elements and depleted in HFSEs such as Nb (10.0–14.0 ppm), Ta (0.81–1.10 ppm), and P (740–1000 ppm) (Figure 4b). In addition, the diorite rocks had lower Sr/Y values (5.81–9.01) and $(La/Yb)_N$ values (5.8–7.0) and higher Y values (21.1–23.4 ppm), which were obviously different from the geochemical characteristics of the adakite rocks, but similar to the typical arc calc–alkaline rocks [41].

4.2. Zircon U–Pb Geochronology

Sample (BHG–N1) is a monzogranitic breccia collected from the Binghugou deposit. The zircons are mainly prismatic and euhedral shapes, with the aspect ratio mostly in the range of 1:1–2:1, and typical oscillatory zones are common (Figure 5a). Th/U ratios are less than 1, except for one result (=1.43), which was consistent with the characteristics of typical magmatic zircons [42]. Fifteen analyses from this sample yielded $^{207}Pb/^{206}Pb$ ages from 2476 to 2551 Ma (Table 3), defining a weighted mean age of 2498.2 ± 7.5 Ma (mean squared weighted deviation (MSWD) = 0.103) (Figure 6a).

Sample (DJG–N1) is monzogranite collected from the Dajiagou deposit. Most zircons exhibited oscillatory or planar zoning under CL, and the grain size in the range of 100–150 μm with the aspect ratio of 1:1–2:1 (Figure 5b). The Th/U ratios of zircon are mostly 0.44–0.82, characteristic of magmatic zircon. The $^{207}Pb/^{206}Pb$ age of 14 zircon grains ranges from 2513 to 2550 Ma (Table 3), with the weighted mean age of 2544.7 ± 8.8 Ma (MSWD = 0.09) (Figure 6b).

Sample (DJG–N2) is diorite collected from the Dajiagou deposit. The shape of zircon is mainly stubby prismatic. The zircons are translucent with a grain size of 80–130 μm, and the aspect ratio of 1:1–2:1. Most zircons had typical magmatic oscillation zoning (Figure 5c), and Th/U ratios at 0.14–0.88, indicating that the zircons were magmatic zircons. Thirteen zircon grains yielded concordant $^{206}Pb/^{238}U$ age of 151 ± 2 to 182 ± 3 Ma (Table 3), with a weighted mean of 169.7 ± 5.1 Ma (MSWD = 0.118) (Figure 6c).

Sample (DXG–N1) is monzogranite collected from the Daxigou deposit. The zircons were mainly prismatic in shape and a few are irregular. The grain size ranges from 100 to 130 μm and the aspect ratio is 1:1–1:2. Most of the zircons are dark, with internal oscillation zoning (Figure 5d). The Th/U ratios (0.10–1.09) exhibit the characteristics of magmatic zircons. The $^{207}Pb/^{206}Pb$ ages of the 16 zircon grains range from 2492 to 2507 Ma (Table 3) and yielded a weighted mean age of 2501.7 ± 8.3 Ma (MSWD = 0.076) (Figure 6d).

Sample (GLG–N1) is monzogranite collected from the Gaoligou deposit. Most zircon grains are euhedral and elongate with lengths of 90–150 μm and aspect ratio of 1:1 to 1:2. The zircons are mostly translucent with clear magmatic oscillation zoning in the CL images, indicating a magmatic origin (Figure 5e). The 12 analyses show $^{207}Pb/^{206}Pb$ ages from 2445 to 2467 Ma (Table 3) and yielded a weighted mean age of 2458.0 ± 11.0 Ma (MSWD = 0.11) (Figure 6e).

Sample (ZMG–N1) is trondhjemite collected from the Zhemagou deposit. The zircon grains are subhedral to euhedral, with lengths of 80–130 μm and aspect ratio of 1–2. Most zircons have typical oscillation zoning (Figure 5f) and the Th/U ratios are between 0.35 and 1.01, indicating magmatic origin. The $^{207}Pb/^{206}Pb$ ages of 15 analytical spots on the zircon grains range from 2489 to 2511 Ma (Table 3), with a weighted mean age of 2500.4 ± 8.3 Ma (MSWD = 0.180) (Figure 6f).

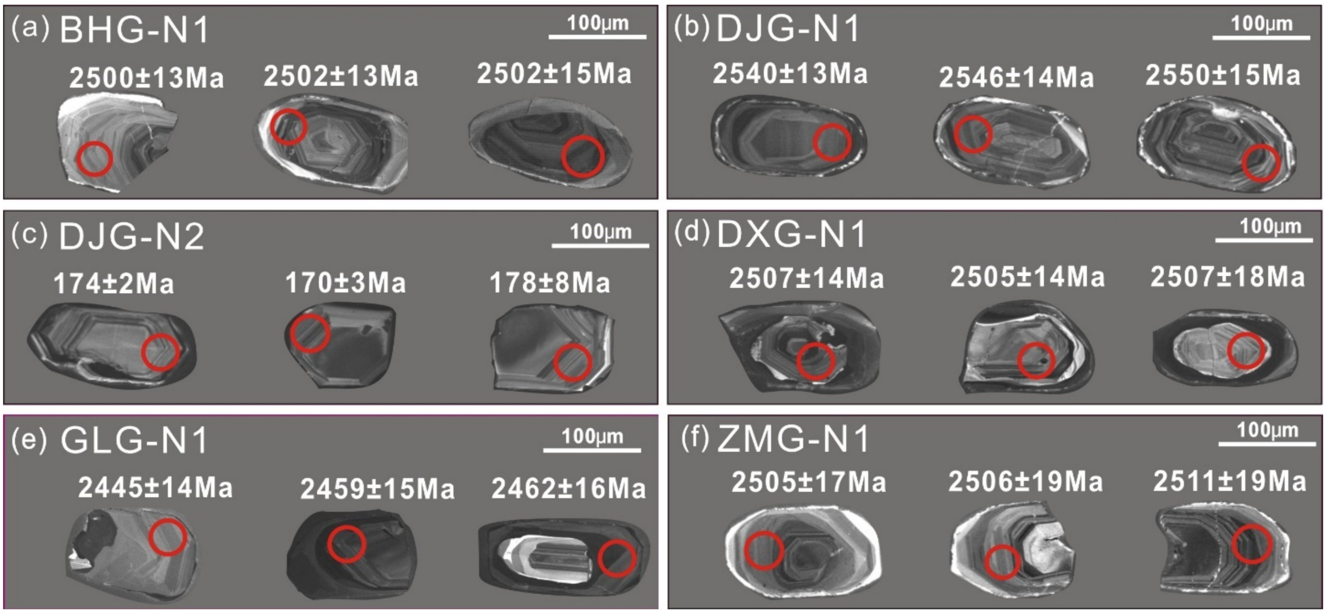

Figure 5. Cathodoluminescence (CL) images of represented analyzed zircons from the TTG gneisses and diorite samples in the Liuhe orefield.

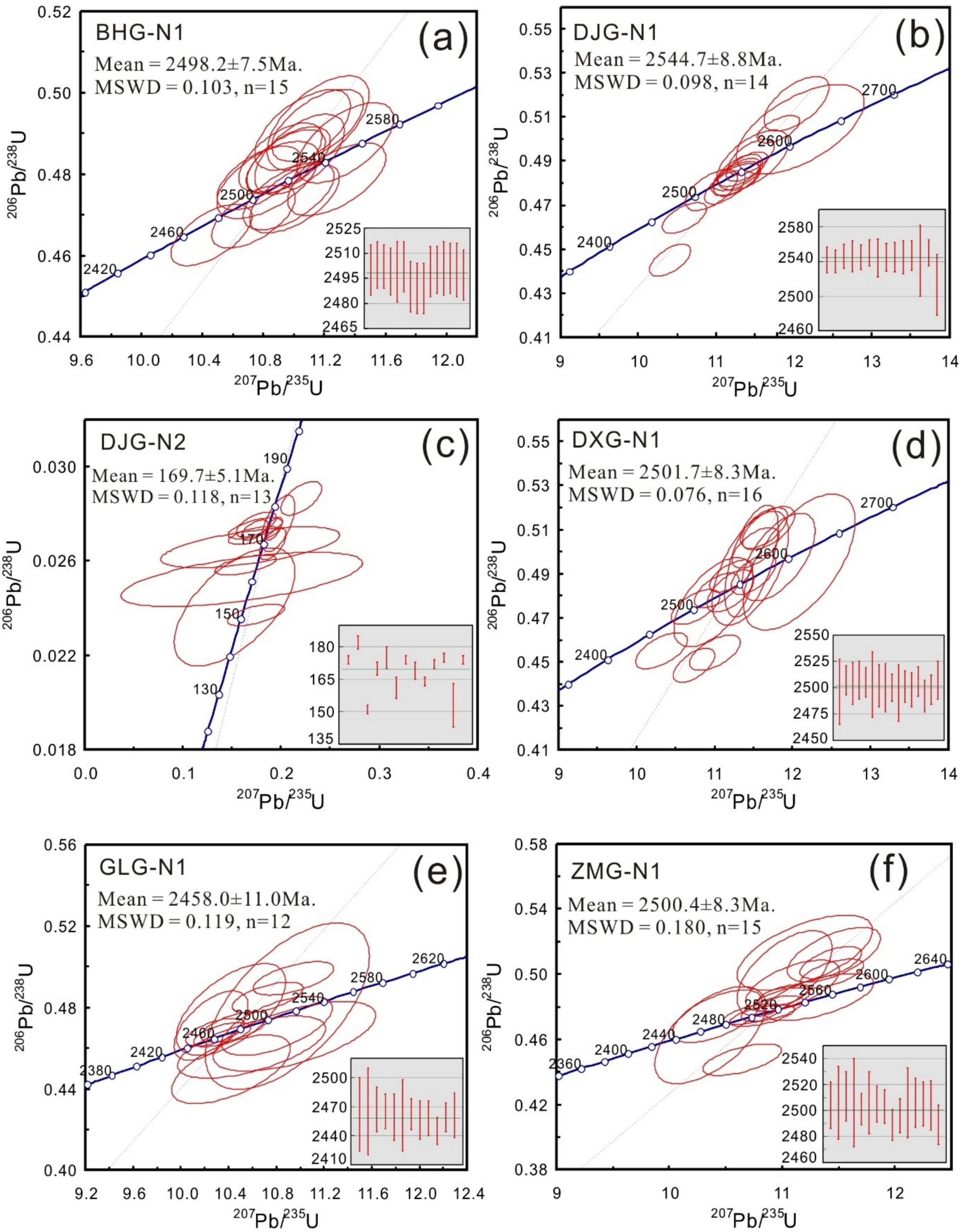

Figure 6. Concordant diagrams showing U–Pb data and mean age of zircons from the Liuhe orefield, NE China.

Table 3. Results of LA-ICPMS U–Pb dating for the single-grain zircon from the TTG gneisses and diorite samples in the Liuhe orefield.

Analysis	Content (ppm)				Isotopic Ratios						Isotopic Ages (Ma)					
No.	Pb	Th	U	Th/U	$^{207}Pb/^{206}Pb$	1σ	$^{207}Pb/^{235}U$	1σ	$^{206}Pb/^{238}U$	1σ	$^{206}Pb/^{238}U$	1σ	$^{207}Pb/^{235}U$	1σ	$^{207}Pb/^{206}Pb$	1σ
BHG-N1-01	894	583	1404	0.42	0.1642	0.0025	11.1560	0.1981	0.4920	0.0058	2579	25	2536	17	2500	15
BHG-N1-02	364	448	470	0.95	0.1645	0.0029	11.0371	0.1941	0.4848	0.0065	2548	28	2526	16	2503	14
BHG-N1-03	388	486	495	0.98	0.1645	0.0023	10.9476	0.1712	0.4830	0.0052	2541	23	2519	15	2502	13
BHG-N1-04	530	338	820	0.41	0.1642	0.0026	10.9105	0.1794	0.4840	0.0056	2545	24	2516	15	2499	14
BHG-N1-05	443	522	606	0.86	0.1642	0.0028	10.8297	0.2213	0.4785	0.0062	2521	27	2509	19	2499	18
BHG-N1-06	315	357	424	0.84	0.1644	0.0028	11.0576	0.2071	0.4908	0.0065	2574	28	2528	17	2502	15
BHG-N1-07	501	463	686	0.67	0.1633	0.0029	11.1577	0.2203	0.4925	0.0076	2581	33	2536	18	2490	15
BHG-N1-08	333	541	379	1.43	0.1632	0.0023	10.7701	0.1821	0.4790	0.0051	2523	22	2503	16	2489	15
BHG-N1-09	359	310	556	0.56	0.1632	0.0024	10.4596	0.1748	0.4650	0.0050	2462	22	2476	15	2489	15
BHG-N1-13	349	458	464	0.99	0.1642	0.0026	10.7350	0.1815	0.4695	0.0051	2481	22	2500	16	2499	15
BHG-N1-14	328	357	463	0.77	0.1642	0.0025	10.9651	0.1800	0.4834	0.0054	2542	23	2520	15	2500	14
BHG-N1-15	1191	1448	1567	0.92	0.1644	0.0037	11.2804	0.2128	0.4787	0.0059	2522	26	2547	18	2501	16
BHG-N1-16	1213	542	2065	0.26	0.1644	0.0033	11.0038	0.1940	0.4740	0.0056	2501	24	2523	16	2501	15
BHG-N1-17	1140	860	1810	0.48	0.1642	0.0034	10.9652	0.1960	0.4746	0.0054	2504	24	2520	17	2500	16
BHG-N1-18	1177	1140	1655	0.69	0.1639	0.0032	11.3370	0.2098	0.4876	0.0065	2560	28	2551	17	2497	15
DJ-N1-01	551	625	796	0.79	0.1685	0.0027	11.2825	0.2099	0.4836	0.0062	2543	27	2547	17	2542	15
DJ-N1-02	1094	1158	1632	0.71	0.1682	0.0025	11.1141	0.1713	0.4779	0.0050	2518	22	2533	14	2540	13
DJ-N1-03	650	597	958	0.62	0.1689	0.0024	11.3940	0.1743	0.4874	0.0044	2560	19	2556	14	2546	14
DJ-N1-05	671	476	1073	0.44	0.1689	0.0030	11.2571	0.2082	0.4816	0.0048	2534	21	2545	17	2546	18
DJ-N1-07	499	495	714	0.69	0.1687	0.0026	11.4563	0.1917	0.4919	0.0054	2579	23	2561	16	2545	14
DJ-N1-08	489	462	683	0.68	0.1692	0.0025	11.8007	0.1806	0.5045	0.0041	2633	18	2589	14	2550	15
DJ-N1-09	1830	4735	2932	1.61	0.1687	0.0028	11.4704	0.3046	0.4904	0.0090	2573	39	2562	25	2544	22
DJ-N1-12	465	435	670	0.65	0.1687	0.0026	11.2964	0.1830	0.4848	0.0042	2548	18	2548	15	2545	16
DJ-N1-14	574	649	788	0.82	0.1687	0.0053	10.9389	0.2191	0.4768	0.0061	2513	27	2518	19	2545	17
DJ-N1-15	678	500	1081	0.46	0.1688	0.0030	12.0319	0.2751	0.5160	0.0082	2682	35	2607	21	2545	19
DJ-N1-16	650	637	907	0.70	0.1689	0.0030	11.2652	0.1971	0.4831	0.0043	2541	19	2545	16	2547	17
DJ-N1-17	503	463	667	0.69	0.1684	0.0065	12.0803	0.5406	0.5044	0.0134	2633	58	2611	42	2541	41
DJ-N1-18	1138	1218	2013	0.61	0.1692	0.0027	10.4080	0.1746	0.4449	0.0048	2373	21	2472	16	2550	15
DJ-N1-19	475	423	721	0.59	0.1688	0.0023	10.8868	0.1546	0.4667	0.0044	2458	20	2488	16	2513	35
DJ-N2-01	121	1428	2753	0.52	0.0790	0.0057	0.3242	0.0163	0.0286	0.0004	174	2	162	8	219	36
DJ-N2-02	31	592	804	0.74	0.0565	0.0033	0.2208	0.0137	0.0287	0.0005	182	3	203	11	193	45
DJ-N2-03	127	1223	2598	0.47	0.1510	0.0035	0.5645	0.0132	0.0271	0.0003	151	2	163	17	320	175
DJ-N2-05	14	245	441	0.56	0.0534	0.0027	0.1917	0.0090	0.0267	0.0004	170	3	178	8	169	49

Table 3. *Cont.*

Analysis	Content (ppm)				Isotopic Ratios						Isotopic Ages (Ma)					
No.	Pb	Th	U	Th/U	^{207}Pb/^{206}Pb	1σ	^{207}Pb/^{235}U	1σ	^{206}Pb/^{238}U	1σ	^{206}Pb/^{238}U	1σ	^{207}Pb/^{235}U	1σ	^{207}Pb/^{206}Pb	1σ
DJ-N2-06	560	2233	15,550	0.14	0.0387	0.0025	0.1972	0.0112	0.0276	0.0008	175	5	183	9	195	41
DJ-N2-07	35	289	642	0.45	0.0663	0.0109	0.4053	0.0943	0.0273	0.0006	161	5	151	71	229	52
DJ-N2-09	23	296	750	0.40	0.0515	0.0016	0.1925	0.0058	0.0274	0.0003	174	2	179	5	169	31
DJ-N2-12	90	854	1890	0.45	0.0546	0.0056	0.3363	0.0650	0.0280	0.0005	169	4	158	52	187	41
DJ-N2-13	133	1507	2067	0.73	0.0737	0.0050	0.4435	0.0345	0.0283	0.0004	164	2	154	18	216	127
DJ-N2-14	139	1596	2674	0.60	0.0552	0.0049	0.2727	0.0140	0.0280	0.0003	172	2	161	14	195	50
DJ-N2-16	75	804	1338	0.60	0.0443	0.0044	0.2412	0.0139	0.0281	0.0004	175	2	164	12	88	34
DJ-N2-18	44	870	991	0.88	0.1274	0.0130	0.4997	0.0542	0.0271	0.0019	153	10	144	36	193	33
DJ-N2-19	89	960	1749	0.55	0.0494	0.0038	0.2674	0.0171	0.0282	0.0003	174	2	163	16	265	129
DXG-N1-02	590	549	801	0.68	0.1639	0.0057	11.4763	0.2258	0.4958	0.0168	2596	72	2563	18	2496	31
DXG-N1-03	233	192	352	0.55	0.1649	0.0041	11.2062	0.1986	0.4821	0.0063	2537	27	2540	17	2507	14
DXG-N1-05	1333	258	2649	0.10	0.1646	0.0054	10.3210	0.2189	0.4551	0.0054	2418	24	2464	20	2504	20
DXG-N1-08	538	737	685	1.08	0.1650	0.0041	11.0063	0.2164	0.4541	0.0053	2414	23	2524	18	2507	18
DXG-N1-09	277	187	453	0.41	0.1647	0.0040	10.7387	0.1753	0.4485	0.0051	2388	23	2501	15	2505	14
DXG-N1-10	697	467	1047	0.45	0.1646	0.0067	12.0867	0.4739	0.4953	0.0204	2594	88	2611	37	2503	31
DXG-N1-11	773	547	986	0.56	0.1645	0.0047	11.8219	0.3089	0.4975	0.0131	2603	56	2590	24	2502	20
DXG-N1-12	442	408	645	0.63	0.1643	0.0110	10.9867	0.3347	0.4771	0.0134	2515	58	2522	28	2500	23
DXG-N1-13	369	285	541	0.53	0.1642	0.0039	11.4992	0.1902	0.4895	0.0059	2569	26	2565	15	2500	13
DXG-N1-14	322	421	386	1.09	0.1637	0.0060	11.4618	0.3241	0.4925	0.0171	2582	74	2561	26	2495	27
DXG-N1-15	439	449	638	0.70	0.1643	0.0031	11.0255	0.1890	0.4824	0.0052	2537	23	2525	16	2501	15
DXG-N1-16	797	749	1144	0.66	0.1641	0.0030	11.6934	0.2218	0.5106	0.0065	2659	28	2580	18	2498	16
DXG-N1-17	822	662	1211	0.55	0.1648	0.0025	11.6370	0.2008	0.5107	0.0061	2660	26	2576	16	2506	14
DXG-N1-18	845	930	1146	0.81	0.1634	0.0028	11.2149	0.1836	0.4890	0.0048	2566	21	2541	15	2492	15
DXG-N1-19	1418	1490	1988	0.75	0.1641	0.0028	11.5269	0.1996	0.5017	0.0061	2621	26	2567	16	2498	14
DXG-N1-20	156	180	219	0.82	0.1649	0.0032	10.7565	0.2053	0.4749	0.0052	2505	23	2502	18	2507	18
GLG-N1-08	4736	1844	1880	0.98	0.1606	0.0057	10.9528	0.4493	0.4658	0.0113	2465	50	2519	38	2462	38
GLG-N1-09	2321	1771	1381	1.28	0.1609	0.0076	10.8937	0.4534	0.4805	0.0270	2529	117	2514	39	2465	45
GLG-N1-10	3207	1809	957	1.89	0.1610	0.0091	10.8057	0.3073	0.4709	0.0096	2488	42	2507	26	2467	23
GLG-N1-11	4209	1852	1821	1.02	0.1609	0.0060	10.2539	0.2048	0.4710	0.0112	2488	49	2458	18	2465	18
GLG-N1-12	3145	1575	1257	1.25	0.1603	0.0074	10.4204	0.3281	0.4496	0.0112	2393	50	2473	29	2459	24
GLG-N1-13	2828	1463	1145	1.28	0.1605	0.0095	10.5932	0.4095	0.4605	0.0101	2442	44	2488	36	2461	37
GLG-N1-15	4184	1338	2587	0.52	0.1606	0.0026	10.4513	0.1877	0.4704	0.0050	2485	22	2476	17	2462	16
GLG-N1-16	2047	1109	1075	1.03	0.1601	0.0029	10.9438	0.2232	0.4942	0.0054	2589	23	2518	19	2456	20

Table 3. *Cont.*

Analysis	Content (ppm)				Isotopic Ratios						Isotopic Ages (Ma)					
No.	Pb	Th	U	Th/U	$^{207}Pb/^{206}Pb$	1σ	$^{207}Pb/^{235}U$	1σ	$^{206}Pb/^{238}U$	1σ	$^{206}Pb/^{238}U$	1σ	$^{207}Pb/^{235}U$	1σ	$^{207}Pb/^{206}Pb$	1σ
GLG-N1-17	1504	854	872	0.98	0.1602	0.0028	10.7276	0.1964	0.4849	0.0049	2548	21	2500	17	2458	18
GLG-N1-18	1185	723	804	0.90	0.1590	0.0023	10.2866	0.1620	0.4678	0.0044	2474	19	2461	15	2445	14
GLG-N1-19	874	593	687	0.86	0.1603	0.0024	10.3462	0.1584	0.4666	0.0039	2469	17	2466	14	2459	15
GLG-N1-20	677	482	696	0.69	0.1605	0.0076	10.4213	0.3030	0.4789	0.0149	2522	65	2473	27	2461	23
ZMG-N1-01	626	444	994	0.45	0.1647	0.0043	11.4605	0.2729	0.5120	0.0110	2665	47	2561	22	2504	18
ZMG-N1-05	1235	1368	1743	0.78	0.1649	0.0042	11.0217	0.2785	0.5005	0.0173	2616	74	2525	24	2506	28
ZMG-N1-07	725	663	1023	0.65	0.1653	0.0093	10.6449	0.2304	0.4475	0.0064	2384	28	2493	20	2511	19
ZMG-N1-08	905	530	1495	0.35	0.1648	0.0046	10.3615	0.3247	0.4626	0.0197	2451	87	2468	29	2506	34
ZMG-N1-09	1034	1284	1310	0.98	0.1643	0.0027	11.4326	0.1798	0.5071	0.0065	2644	28	2559	15	2501	12
ZMG-N1-10	890	630	1387	0.45	0.1649	0.0041	11.3242	0.3231	0.4860	0.0095	2553	41	2550	27	2506	24
ZMG-N1-11	813	597	1269	0.47	0.1648	0.0026	10.9127	0.1810	0.4788	0.0052	2522	23	2516	15	2505	14
ZMG-N1-12	589	468	863	0.54	0.1645	0.0027	11.4420	0.1855	0.5004	0.0058	2615	25	2560	15	2503	13
ZMG-N1-13	1213	940	1869	0.50	0.1632	0.0022	11.0125	0.1535	0.4870	0.0045	2557	20	2524	13	2489	12
ZMG-N1-14	971	1256	1244	1.01	0.1639	0.0023	10.9980	0.1646	0.4844	0.0048	2546	21	2523	14	2496	13
ZMG-N1-16	657	418	1090	0.38	0.1649	0.0082	11.2016	0.3964	0.5132	0.0151	2670	64	2540	33	2506	27
ZMG-N1-17	988	876	1469	0.60	0.1648	0.0042	11.0940	0.2746	0.4929	0.0104	2583	45	2531	23	2506	19
ZMG-N1-18	1945	1913	2865	0.67	0.1648	0.0029	10.8228	0.1894	0.4746	0.0044	2504	19	2508	16	2505	17
ZMG-N1-19	707	681	1053	0.65	0.1646	0.0089	10.4246	0.2614	0.4742	0.0106	2502	46	2473	23	2504	19
ZMG-N1-20	612	421	969	0.43	0.1632	0.0024	10.7373	0.1671	0.4755	0.0042	2508	19	2501	14	2489	15

5. Discussion

5.1. Timing of Magmatism in the Liuhe Gold Ore Field

There are some controversies about the timing of gold deposits in the Jiapigou gold belt, with interpreted ages ranging from the Neoarchaean–Palaeoproterozoic, 2475–2469 Ma [17,43], through the Indo-Chinese epoch of the Mesozoic, 204 Ma [44], to the Yanshannian epoch of the Mesozoic, 170–160 Ma [45–48]. Other scholars have proposed a multi-stage mineralization, 3000–2800 Ma, 2700–2500 Ga, 2000–1800 Ma, 500–300 Ma, 230–130 Ma [49–51]. Huang (2012) [52] suggested that the gold mineralization of the Jiapigou gold belt first took place during the Palaeoproterozoic Era (~2426.0 Ma). The Yanshanian gold mineralization event (~166.2 Ma) may also have a major effect on the ore bodies of the Jiapigou gold belt, and this led to new gold mineralization as well as redistribution of the Palaeoproterozoic ore bodies.

The zircon U–Pb dating provides constraints on the formation ages of ore-hosting TTGs. The zircon $^{207}Pb/^{206}Pb$ ages of ore-hosting TTGs from the GLG, DXG, ZMG, and BHG deposits were 2458.0 $\pm$ 11.0, 2501.7 $\pm$ 8.3, 2500.4 $\pm$ 8.3, and 2498.2 $\pm$ 7.5 Ma, respectively. The age of these ore-hosting granites may indicate a large-scale magmatic event in the Liuhe orefield in late Neoarchean to early Paleoproterozoic. The zircon $^{206}Pb/^{238}U$ age obtained for the ore-hosting fine-grained diorite of the DJG deposit is 169.7 $\pm$ 5.1 Ma, indicating that magmatism took place in the early Jurassic. Based on the above data, we propose that emplacement of ore-hosting magma in the Liuhe orefield mainly took place in two epochs: late Neoarchean to early Paleoproterozoic and early Jurassic of Mesozoic.

5.2. Petrogenesis of Archean TTG Series

In the samples collected in this study, except for the diorite in the Dajiagou deposit, all the trondhjemite and monzogranite (monzogranite breccia) belonged to Archean TTG gneisses with relatively clear petrological characteristics, and most of them are of gneissic and/or streaked structure. The mineral composition was quartz + plagioclase (oligoclase) + potassium feldspar + biotite + amphibole. In the TAS classification diagram (Figure 7a), 4 of the 18 samples fell into the diorite field, 10 into the granodiorite, and 4 into the granite. This indicates that most of the TTG rocks belong to the granodiorite [53]. The major elements show a linear distribution in the Harker diagram (Figure 8); SiO_2 has negative correlations with MgO, TiO_2, Fe_2O_3, CaO, and P_2O_5, reflecting the characteristics of typical magmatic evolution, while K_2O, Na_2O, and Al_2O_3 have no significant correlations with SiO_2, showing the characteristics of Archean TTG rocks. According to the molar ratios of $Al_2O_3/(CaO + Na_2O + K_2O)$ and $Al_2O_3/(Na_2O + K_2O)$, most samples are peraluminous, with a few samples being metaluminous in the A/CNK vs. A/NK diagram (Figure 7b) [54]. In the K_2O vs. SiO_2 diagram (Figure 7c), except for a few samples, most fell into the high-K calc–alkaline series and calc–alkaline series, indicating that they were calc–alkaline series rocks [55]. In the Nb vs. 10,000 $\times$ Ga/Al diagram, all samples were plotted within the fields of I- and S-type granites (Figure 7d), indicating that the TTG rocks have an affinity to those of the I-type suite [56]. The trondhjemite and monzogranite have similar REE distribution patterns, both of which show that the fractionation degree of light and heavy REEs increases gradually, indicating that they belong to a homologous magmatic evolution process and the magmatic differentiation degree gradually increases [57,58].

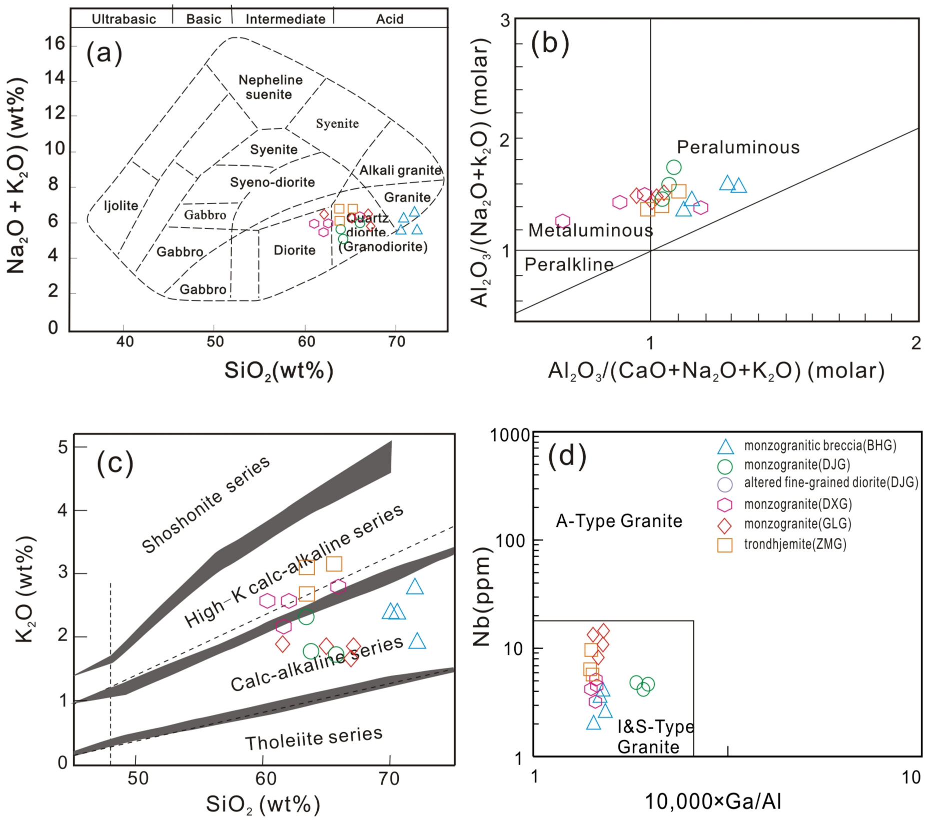

Figure 7. (**a**) The chemical classification and nomenclature of plutonic rocks using the total alkalis versus silica (TAS) diagram [53]; (**b**) A/NK vs. A/CNK [54]; (**c**) K_2O vs. SiO_2 [55]; (**d**) diagrams of Nb vs. 10,000 × Ga/Al of A-type granites from I- and S-type granites [56].

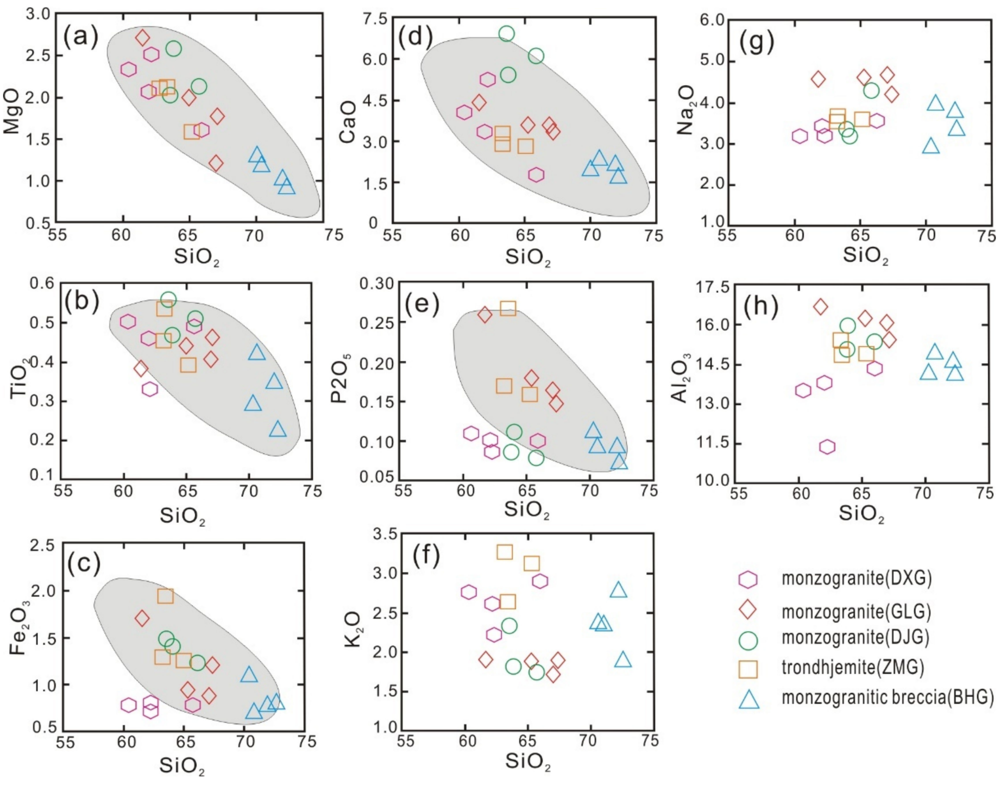

Figure 8. Harker variation diagrams for the TTG gneisses in the Liuhe deposits.

Adakite is a petrological term introduced to refer to a special type of island-arc andesite, dacite, rhyolite (dacite is the most common), or tonodiorite and trondhjemite in the Cenozoic island-arc environment associated with the young subducted oceanic lithosphere [59,60]. The geochemical characteristics of the adakites are $SiO_2 \geq 56\%$ and $Al_2O_3 \geq 15\%$, and MgO is usually less than 3% (rarely more than 6%). They are rich in Na+, with Na_2O and K_2O contents in the range of ±4 and ±1–2%, generally $Na_2O > K_2O$. The contents of Y and Yb are relatively low, at <18 and <1.9 ppm, respectively. It shows positive Eu and Sr anomalies, with the Sr > 400 ppm. Adakite is formed by the partial melting of slab during subduction at a small angle and is used as a marker to identify subduction. The TTG rocks in the study area exhibited the following characteristics: SiO_2 content varied from 62.99 to 70.67%, with higher $A1_2O_3$ (12.58 to 15.71%) and Na_2O/K_2O ratios (1.16 to 2.9), and lower MgO (0.93 to 2.73%) and Mg# value. Trace elements showed a positive Eu anomaly and low Y and Yb content, and the Sr/Y ratios were high (22.3–79.6). The TTGs fall into the adakite field according to the Sr/Y–Y discriminant diagram (Figure 9a) [61], indicating that they belong to the modern island-arc adakite rocks [52].

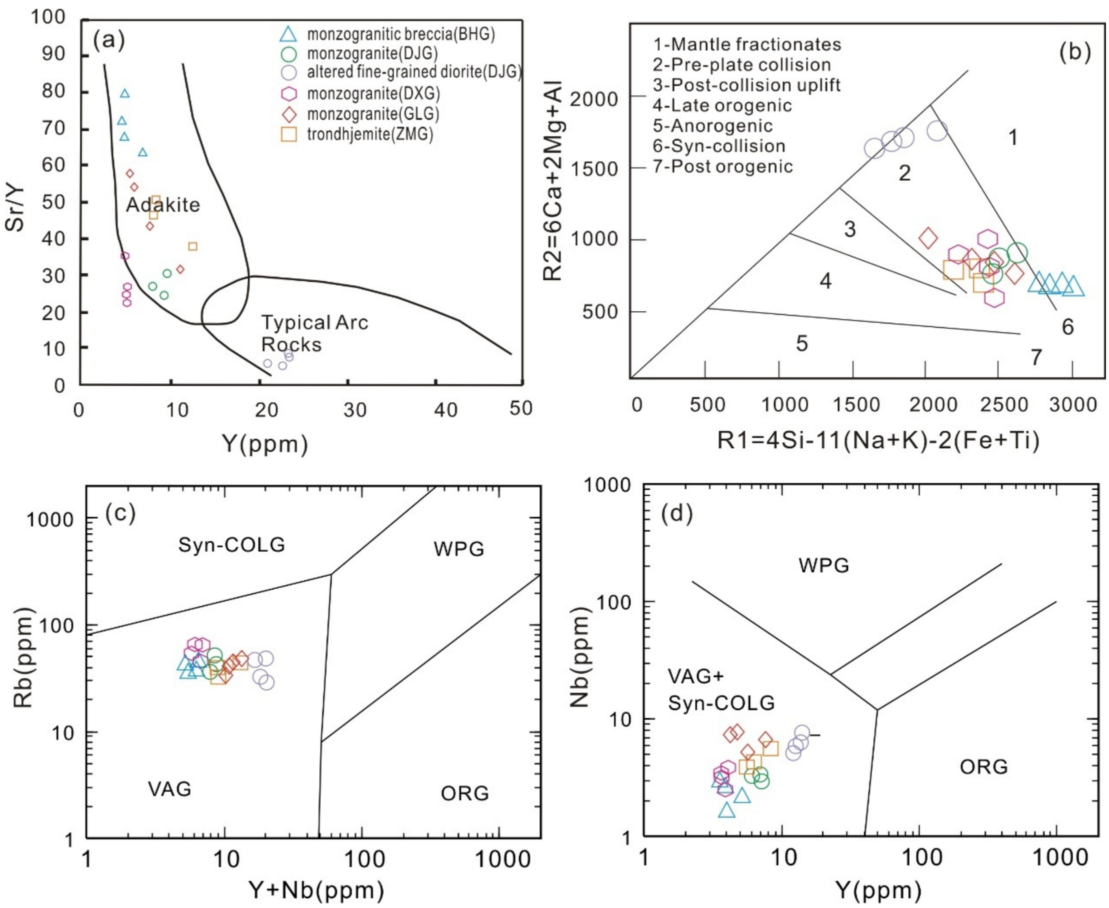

Figure 9. (**a**) Sr/Y-Y diagrams for the dioritic gneisses adapted from Martin (1999) [61]; (**b**) R1 vs. R2 diagram (after Batchelor et al., 1985; Qu et al., 2004) [62,63], R1 = 4Si − 11(Na + K) − 2(Fe + Ti) (mol), R2 = 6Ca + 2 Mg + Al (mol); Discrimination diagrams for granitic rocks after Pearce et al. (1984) [64], (**c**) Rb-Y + Nb diagram and (**d**) Nb-Y diagram. VAG: volcanic-arc granites; syn-COLG: syn-collisional granites; WPG: within plate granites; ORG: ocean-ridge granites.

At the same time, the Neoarchean TTG in the study area had high SiO_2, while Mg#, Cr and Ni were low, indicating that the parent magma of the Neoarchean TTG did not interact with the mantle peridotite; the magma was mainly derived from the dehydration and partial melting of garnet amphibolite, and the contribution of mantle components was not obvious [65]. Because the temperature of the Archean mantle was much higher than that of the present, the softening and melting of the Archean oceanic crust occurred once subduction took place, making the subduction of the Archean ocean plate quite different from that of the modern ocean plate, and low angle gentle subduction occurred in the majority of cases [61]. The thin or undeveloped mantle wedge above the gently subducted oceanic crust resulted in a small contribution of mantle components to Archean TTG rocks, generally showing low Mg# values. The major rock formations of the Archean are composed of greenstone belt and TTG gneiss. The widespread occurrence of olivine komatiites in greenstone belts around the world indicates that the temperature of the Archean mantle and the melting degree of mantle magma were much higher than today. Therefore, the average composition of the Archean oceanic crust was also more basic than that of the present, and it can be inferred that the magma produced by the melting of mantle or oceanic crust caused by Archean plate subduction was also more basic than that of island-arc volcanic rocks currently. The partial melting of mafic rocks in the lower crust caused by basaltic magma underplating is the main mechanism for the formation of granitic rocks in the modern island arcs and active continental margins. The TTG rocks in the study area contained amphibolite inclusions with different basic degrees, which were metamorphosed by the products of basaltic magma underplating the subduction background. Based on the above analysis, we suggest that the TTG series in the study area may have derived from the partial melting of mafic lower crustal caused by the underplating of basaltic magma on the island-arc or active continental margin, and its formation is similar to the current generation mechanism of granitic magma under the same tectonic setting.

5.3. Tectonic Setting of the Magmatism in the Liuhe Area

The Neoarchean TTG rock series from the Liuhe area is a series of intermediate-acidic metaluminous–peraluminous calc–alkaline rocks, and their geochemical characteristics are close to those of the island-arc or continental margin-arc setting in the Phanerozoic [54]; most of the samples fell into the adakite area in the Sr/Y–Y discrimination diagram [66]. From the perspective of structural geology, adakite can be used as a magmatic marker to identify the subduction zone [67]. Relevant studies have pointed out that the NCC is different from the ancient continental crust and has the characteristics of island arc [68] and thus inferred that tectonism similar to modern plate subduction had occurred in the Mesoarchean. Although the oldest rocks found in the NCC were quartzite and felsic gneiss, the island-arc attribute of the initial continental crust does not exclude the early continental crust having a horizontal accretion mode, that is, the vast cratonic continental block formed by a series of island-arc collisions and aggregations [69]. Geng et al. (2012) [70] also noted that the formation of TTG intrusive rocks in the NCC was about 100 Ma earlier than regional metamorphism, which can be explained by the collision process after subduction. The emplacement age of TTG rock was 2515–2551 Ma in this study, which was basically consistent with the previous results, indicating that there was intense and extensive magmatism in the Liuhe area at the end of the Neoarchean [71,72]. According to the R1–R2 discrimination diagram (Figure 9b), the collected samples were mainly plotted in the area of pre-plate collision [58,61]. Nearly all the rocks fell in the VAG field in the Rb–Y + Nb diagram (Figure 9c), [and the VAG + Syn–COLG field in the Nb–Y diagram (Figure 9c) [62]. All samples were far from within-plate granite (WPG) and ocean-ridge granite (ORG) areas, indicating that the magmatism was related to plate subduction. The above features suggested a subduction-related arc signature, and it is widely accepted that the TTG rocks were derived from subducted oceanic crust [73]. Therefore, the Neoarchean ore-bearing TTG series in the Liuhe area was likely formed in an island-arc or active continental margin setting before plate collision.

The formation of metamorphic plutonic intrusive rocks indicated that the Liuhe area had experienced the formation, thickening, collision–subduction, and melting of the ancient continental crust in the Neoarchean–Paleoproterozoic, reflecting the continuous growth and maturation of the Archean crust. The source of partial melting gradually moved upward from the early upper mantle to the lower crust and upper crust and represented an important process of continental crust horizontal accretion in the late Neoarchean [74]. In the Precambrian crustal evolution of the North China plate, ca. 2.6 Ga was the period in which various geological processes occurred intensively, and ca. 2.5 Ga was the main activity period of TTG magma.

Under the subduction of the Pacific plate in the Mesozoic, the eastern part of China was characterized by intense volcanic eruption, magmatic intrusion, and tectonic movement. Because of the northwest migration, subduction, and collision of the Pacific plate, the North China plate has undergone a remarkable counterclockwise rotation. The tectonic stress in this area is manifested as the sinistral translation of the NE-trending Dunmi fault and its secondary Liangjiang fault, leading to large-scale regional folding of the existing Jiapigou fault in the process of sinistral torsion. A series of tensional NNE–NE-trending faults are derived at the turning end of the fold, while the NS-trending faults are in a compressive state; therefore, there is no NS-trending ore body. Indosinian magmatic activity occurred in the Liuhe area in the early Mesozoic, and the magmatic rocks represented by Wudaokuohe granite body intruded into place. In the Yanshanian, hypabyssal, and ultra-hypabyssal rhyolites, quartz porphyry, granite porphyry, and other magmatic emplacement occurred. The ore-controlling structure of the Jiapigou gold belt, the NW-trending ductile–brittle shear zone, has extended to the Liuhe area in the southeast direction, and the Dajiagou gold deposit is now located in the southeast extension of the ore-controlling structure. At the same time, the subduction of the Pacific plate also formed NE-trending faults, which cut the ductile–brittle shear zone and ore body formed in the earlier period, causing certain damage to the ore body. Therefore, there are relatively few Archean deposits in the Liuhe orefield and even the entire Jiapigou gold belt.

5.4. Archean Gold Transport in the Liuhe Gold Orefield

Considering the theories of Precambrian gold mineralization at home and abroad and the comprehensive research results of the geological characteristics of various gold deposits in the study area [5,48,75–77], we suggest the following scenario for the initial Au enrichment of the Liuhe gold orefield. The metamorphic supracrusts of the late Mesoarchean in this area belong to the basic volcanic formation, accompanied by a small amount of ferrosilicon quartzite sedimentary formation, and it is well known that the Archean basic volcanic formations have gold-bearing properties [3,6,78–81]. The upwelling of mantle under the original Longgang old landmass led to thinning and rifting of the upper crust, and the greenstone belt was formed by the eruption accumulation and clastic deposition of a large number of tholeiite and felsic volcanic rocks [64,82,83]. The subcontinental lithospheric mantle (SCLM) was metasomatized multiple times by Au-enriched melts and fluids before subducting beneath the NCC [84]. Fluids derived from dehydration during the oceanic crust subduction additionally metasomatized the cratonic SCLM with incompatible and fluid-mobile elements, including Au and Pb [85], and the entry of a large amount of subduction fluids not only triggered partial melting of the SCLM, but also provided an effective medium to remove the incompatible elements from the modified SCLM [86–89]. The resulting Au-enriched melt then underplated the cratonic mafic lower continental crust (LCC). With the intensifying of continent–continent collision and arc–continent collision, TTG granitic magma continued its upwelling, emplacement, and anatexis. From the late Neoarchean to early Paleoproterozoic, the intensification of metamorphism and deformation caused the schistosity and mylonization of the metamorphic supracrusts and felsic gneiss, forming a large-scale ductile shear zone in the Liuhe area and even the entire Jiapigou gold ore belt [44,90,91]. With the intensification of tectonic activity and uplift of terrane, the ductile shear zone was transformed into a ductile–brittle shear zone, resulting in the dynamic metamorphism of the initial tectonic cataclasite [92]. A large amount of granite magma rose along the multi-stage large-scale ductile shear zone system, differentiated a large amount of magmatic fluid, mixed with the fluid enriched in ore-forming materials, and activated the Au in the gold-bearing metamorphic rocks, then migrated to the shear zone through the water–rock interaction [93,94]. Under these conditions, shallow water and metamorphic hydrothermal fluids circulated and migrated along the tectonic belt owing to the development of rock fissures and the increase in porosity, causing the rocks in the tectonic belt to undergo the intergranular dialysis, which triggered further activation and migration of gold [43,63]. By using the secondary structure of the ductile shear zone as the ore hosting, the ore-forming materials were enriched and precipitated, and eventually formed gold ore bodies (Figure 10).

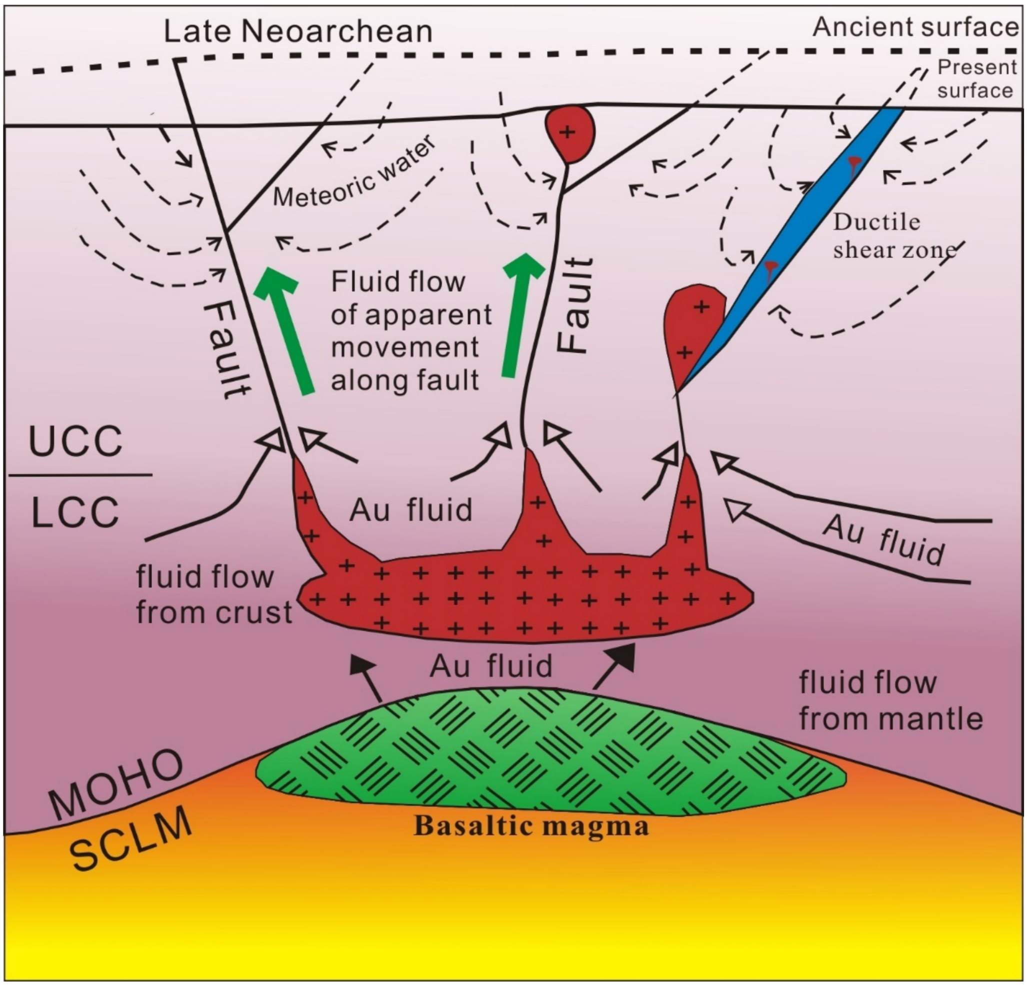

Figure 10. Gold mineral transport model within Neoarchean TTG in the Liuhe orefield (after [95]). UCC-upper continental crust; LCC-lower continental crust; SCLM-subcontinental lithospheric mantle.

6. Conclusions

1. The zircon ages of ore-hosting TTGs and fine-grained diorite indicated that the large-scale ore-hosting magma emplacement in the Liuhe orefield mainly took place in two epochs: late Neoarchean to early Paleoproterozoic and early Jurassic of Mesozoic.
2. The Neoarchean TTGs in the Liuhe area comprise a series of intermediate-acidic metaluminous–peraluminous calc–alkaline rocks, which belong to the modern island-arc adakite rocks.
3. The Ca. 2.5 Ga was the main activity period of TTG magma in the Liuhe area, the ore-hosting TTGs were derived from the partial melting of mafic lower crustal caused by the underplating of basaltic magma on the island-arc or active continental margin before plate collision.
4. The magmatism of the Dajiagou deposit occurred in an active continental margin setting associated with the westward subduction of the paleo-Pacific plate beneath the Eurasian plate during the early Jurassic of Mesozoic period.

Author Contributions: Conceptualization, J.Z.; methodology, Y.Y.; software, W.W.; investigation, J.Z., Y.Y., P.G. and W.W.; data curation, P.G.; writing—original draft preparation, J.Z.; writing—review and editing, J.Z. and Y.Y.; visualization, W.W.; supervision, Y.Y. All authors have read and agreed to the published version of the manuscript.

Funding: This research received no external funding.

Data Availability Statement: The data provided in this study can be obtained from the figures and the tables in the article.

Acknowledgments: The authors are most grateful to the staff of the ALS Chemex, Guangzhou, China, as well as the laboratory of Hebei Institute of Regional Geology and Mineral Resources Survey, Langfang, China and the MLR Key Laboratory of Mineral Resources Evaluation in Northeast Asia, Jilin University, Changchun, China, during the zircon U–Pb dating and geochemical analyses. The authors deeply appreciate the kind and critical constructive comments and suggestions from the editor-in-chief and two anonymous reviewers, which greatly improved the quality of our manuscript.

Conflicts of Interest: The authors declare no conflict of interest.

References

1. Zhang, X.-T.; Sun, J.-G.; Han, J.-L.; Feng, Y.-Y. Genesis and ore-forming process of the Benqu mesothermal gold deposit in the Jiapigou ore cluster, NE China: Constraints from geology, geochronology, fluid inclusions, and whole-rock and isotope geochemistry. *Ore Geol. Rev.* **2021**, *130*, 103956. [CrossRef]
2. Han, J.-L.; Sun, J.-G.; Liu, Y.; Zhang, X.-T.; He, Y.-P.; Yang, F.; Chu, X.-L.; Wang, L.-L.; Wang, S.; Zhang, X.-W.; et al. Genesis and age of the Toudaoliuhe breccia-type gold deposit in the Jiapigou mining district of Jilin Province, China: Constraints from fluid inclusions, H–O–S–Pb isotopes, and sulfide Rb–Sr dating. *Ore Geol. Rev.* **2020**, *118*, 103356. [CrossRef]
3. Hart, C.J.; Goldfarb, R.J.; Qiu, Y.; Snee, L.; Miller, L.D.; Miller, M.L. Gold deposits of the northern margin of the North China Craton: Multiple late Paleozoic-Mesozoic mineralizing events. *Miner. Depos.* **2002**, *37*, 326–351. [CrossRef]
4. Zhou, T.; Goldfarb, R.J.; Phillips, N.G. Tectonics and distribution of gold deposits in China-an overview. *Miner. Depos.* **2002**, *37*, 249–282. [CrossRef]
5. Miao, L.; Qiu, Y.; Fan, W.; Zhang, F.; Zhai, M. Geology, geochronology, and tectonic setting of the Jiapigou gold deposits, southern Jilin Province, China. *Ore Geol. Rev.* **2005**, *26*, 137–165. [CrossRef]
6. Geng, Y.; Liu, F.; Yang, C. Magmatic event at the end of the Archean in eastern Hebei Province and its geological implication. *Acta Geol. Sin.* **2006**, *80*, 819–833.
7. Zhang, Y.; Tang, K. Pre-Jurassic tectonic evolution of intercontinental region and the suture zone between the North China and Siberian platforms. *J. Southeast Asian Earth Sci.* **1989**, *3*, 47–55.
8. Zhao, G.; Zhai, M. Lithotectonic elements of Precambrian basement in the North China Craton: Review and tectonic implications. *Gondwana Res.* **2013**, *23*, 1207–1240. [CrossRef]
9. Nie, F.-J. An overview of gold resources of China. *Int. Geol. Rev.* **1997**, *39*, 55–81. [CrossRef]
10. Liu, S.; Wang, Q.; Groves, D.I.; Wang, Z.; Yang, L.; Wu, Z.; Yu, Z.; Huang, P.; Deng, J. Adoption of a mineral system model in successful deep exploration at Erdaogou, China's deepest gold mine, on the northeastern margin of the North China Craton. *Ore Geol. Rev.* **2021**, *131*, 104060. [CrossRef]
11. Han, J.; Deng, J.; Zhang, Y.; Sun, J.; Wang, Q.; Zhang, Y.; Zhang, X.; Liu, Y.; Zhao, C.; Yang, F.; et al. Au mineralization-related magmatism in the giant Jiapigou mining district of Northeast China. *Ore Geol. Rev.* **2022**, *141*, 104638. [CrossRef]
12. Liu, L.; Yang, X.; Santosh, M.; Wang, G.; Aulbach, S. Initial gold enrichment within a Neoarchean granite-greenstone belt: Evidence from ore-bearing and ore-barren samples in the Jiapigou deposits, NE China. *Ore Geol. Rev.* **2017**, *81*, 211–229. [CrossRef]
13. Cheng, Y.Q. (Ed.) *Regional Geology of China*; Geological Publishing House: Beijing, China, 1994; pp. 1–517.
14. Zhai, M.; Santosh, M. Metallogeny of the North China Craton: Link with secular changes in the evolving Earth. *Gondwana Res.* **2013**, *24*, 275–297. [CrossRef]
15. Qiu, Y.; Groves, D.I.; McNaughton, N.J.; Wang, L.-G.; Zhou, T. Nature, age and tectonic setting of granitoid-hosted orogenic gold deposits of the Jiaodong Peninsula, eastern North China craton, China. *Miner. Depos.* **2002**, *37*, 283–305. [CrossRef]
16. Deng, J.; Yang, L.; Gao, B.; Sun, Z.; Guo, C.; Wang, Q.; Wang, J. Fluid evolution and metallogenic dynamics during tectonic regime transition: Example from the Jiapigou Gold Belt in Northeast China. *Resour. Geol.* **2009**, *59*, 140–152. [CrossRef]
17. Sun, S.L. Simulating experiment on formations and evolutions of the gold deposits and shear zones in Jiapigou region. *Mineral. Dep.* **1995**, *14*, 73–81.
18. Cheng, Y.M.; Li, J.J.; Shen, B.F.; Lu, J.S. *Ore-Forming and Ore-Searching Models for Greenstone Gold Deposits in Ji-Liao Region*; Seismic Publishing House: Beijing, China, 1996; pp. 1–182.
19. Zhai, M.; Yang, J.; Liu, W. Large clusters of gold deposits and large-scale metallogenesis in the Jiaodong Peninsula, Eastern China. *Sci. China Ser. D Earth Sci.* **2001**, *44*, 758–768. [CrossRef]
20. Shen, B.; Zhai, A.; Chen, W.; Yang, C.; Hu, X.; Cao, X.; Gong, X. *The Precambrian Mineralization of China*; Geological Publishing House: Beijing, China, 2006; pp. 40–314.

21. Yu, R.; Sun, J.; Wang, S.; Han, J.; Liu, Y. Neoarchean–early Paleoproterozoic crustal evolution in the Jiapigou terrane in the northeastern part of the North China Craton: Geochemistry, zircon U–Pb dating and Hf isotope constraints from the potassic granitic complex. *Precambrian Res.* **2021**, *364*, 106341. [CrossRef]
22. Safonova, I.Y.; Santosh, M. Accretionary complexes in the Asia-Pacific region. Tracing archives of ocean plate stratigraphy and tracking mantle plumes. *Gondwana Res.* **2014**, *25*, 126–158. [CrossRef]
23. Wu, F.-Y.; Sun, D.-Y.; Ge, W.-C.; Zhang, Y.-B.; Grant, M.L.; Wilde, S.A.; Jahn, B.-M. Geochronology of the Phanerozoic granitoids in northeastern China. *J. Asian Earth Sci.* **2011**, *41*, 1–30. [CrossRef]
24. Zeng, Q.; He, H.; Zhu, R.; Zhang, S.; Wang, Y.; Su, F. Origin of ore-forming fluids of the Haigou gold deposit in the eastern Central Asian Orogenic belt, NE China: Constraints from H-O-He-Ar isotopes. *J. Asian Earth Sci.* **2017**, *144*, 384–397. [CrossRef]
25. BGMRJP (Bureau of Geology and Mineral Resources of Jilin Province). *Regional Geology of Jilin Province*; Geological Publishing House: Beijing, China, 1988; pp. 1–698.
26. Zhao, H.L.; Deng, J.F.; Chen, F.J.; Hu, Q.; Zhao, S.K. Cenozoic volcanism, deep interior process and continental rift basin formation in the northeastern China. *J. China Univ. Geosci.* **1996**, *21*, 615–619.
27. Li, C.D.; Zhang, F.Q.; Miao, C.L. Reconsideration of Seluohe Group in Seluohe area, Jilin Province. *J. Jilin Univ.* **2007**, *37*, 841–847.
28. Shen, B.; Li, J.; Mao, D.; Li, S.; Liu, Z.; Zhang, W.; An, C. *Geology and Metallogenic Prognosis of Jiapigou Gold Deposits in Jilin Province*; Geological Publishing House: Beijing, China, 1998; pp. 1–175.
29. Zhao, G.; Sun, M.; Wilde, S.A.; Li, S. Late Archean to Paleoproterozoic evolution of the North China craton: Key issues revisited. *Precambrian Res.* **2005**, *136*, 177–202. [CrossRef]
30. Li, J.J.; Shen, B.F.; Cheng, Y. Study on geochronology of gold deposits in Jiapigou, Jilin Province. *Acta Geol. Sin.* **1996**, *70*, 335–341.
31. Li, L. Research on Ore-Forming Fluids of Gold Deposits in Jiapigou-Haigou Gold Belt, Jilin Province and Deep-Seated Metallogenic Assessment, China. Doctoral Dissertation, Jilin University, Changchun, China, 2016; pp. 1–244.
32. Huang, Z.X. Tectonics-Fluids-Mineralization System of Jiapigou Gold Belt in Jilin Province, China. Doctoral Dissertation, China University of Geosciences, Wuhan, China, 2012; pp. 1–255.
33. Deng, J.; Yuan, W.; Carranza, E.J.M.; Yang, L.; Wang, C.; Yang, L.; Hao, N. Geochronology and thermochronometry of the Jiapigou gold belt, northeastern China: New evidence for multiple episodes of mineralization. *J. Asian Earth Sci.* **2014**, *89*, 10–27. [CrossRef]
34. Yuan, H.-L.; Gao, S.; Dai, M.-N.; Zong, C.-L.; Günther, D.; Fontaine, G.H.; Liu, X.-M.; Diwu, C.R. Simultaneous determinations of U–Pb age, Hf isotopes and trace element compositions of zircon by excimer laser-ablation quadrupole and multiple-collector ICP-MS. *Chem. Geol.* **2008**, *247*, 100–118. [CrossRef]
35. Wiedenbeck, M.; Alle, P.; Corfu, F.; Griffin, W.L.; Meier, M.; Oberli, F.; von Quadt, A.; Roddick, J.C.; Speigel, W. Three natural zircon standards for U-Th-Pb, Lu-Hf, trace-element and REE analyses. *Geostand. Geoanalytical Res.* **1995**, *19*, 1–23. [CrossRef]
36. Van Achterbergh, E.; Ryan, C.; Jackson, S.; Griffin, W.L. Appendix 3 Data Reduction Software for LA-ICP-MS. In *Laser-Ablation-ICPMS in the Earth Sciences*; Sylvester, P., Ed.; Mineralogical Association of Canada Short Course; Mineralogical Association of Canada: Quebec, QC, Canada, 2001; Volume 29, pp. 239–243.
37. Ludwig, K.R. *ISOPLOT 3.0: A Geochronological Toolkit for Microsoft Excel*; Berkeley Geochronology Center Special Publication: Berkeley, CA, USA, 2003; Volume 4, pp. 1–74.
38. Andersen, T. Correction of common lead in U–Pb analyses that do not report ^{204}Pb. *Chem. Geol.* **2002**, *192*, 59–79. [CrossRef]
39. Sun, S.S.; McDonough, W.F. Chemical and isotopic systematics of oceanic basalts: Implications for mantle composition and processes. *Geol. Soc. Lond. Spec. Publ.* **1989**, *42*, 313–345. [CrossRef]
40. McDonough, W.F.; Sun, S.S. The composition of the earth. *Chem. Geol.* **1995**, *120*, 233–253. [CrossRef]
41. Defant, M.J.; Drummond, M.S. Derivation of some modern arc magmas by melting of young subducted lithosphere. *Nature* **1990**, *347*, 662–665. [CrossRef]
42. Hoskin, P.W.O.; Schaltegger, U. The composition of zircon and igneous and metamorphic petrogensis. *Rev. Mineral. Geochem.* **2003**, *53*, 27–62. [CrossRef]
43. Cheng, Y.M.; Li, J.J.; Shen, B.F. *Metallogenic and Ore Prospecting Models of Greenstone Belts Gold Deposits in Southern Jilin Province and Northern Liaoning Province of China*; Seismological Press: Beijing, China, 1996; pp. 87–91.
44. Luo, Z.K.; Guan, K.; Miao, L. Dating of the dykes and altered sericite in Jiapigou gold ore belt, Jilin province and its gold ore formation age. *Geosciences* **2002**, *16*, 19–25.
45. Wang, Y.W. Advancements in dating methods and study of the metallogenic epoch on gold deposits in China. *Geol. Sci. Technol. Inform.* **1994**, *13*, 53–63.
46. Sun, Z.S.; Feng, Y.M. Main minerogenetic epoch determine and exploratory direction of Jiapigou gold deposit, Jilin. *Acta Geosci. Sin.* **1997**, *18*, 367–372.
47. Dong, D.G.; Kang, B.; Bo, J.R. Metallogenic evolution and time of the Jiapigou gold-concentrated area. *Geol.Explor. Non-ferrous Metals.* **1999**, *8*, 213–219.
48. Shen, Y.C.; Zeng, Q.D.; Xie, H.Y. Location time of gold deposits in Jiapigou Haigou mineralisation zone, Jilin Province. *Gold Sci. Technol.* **1999**, *7*, 19–26.
49. Sun, B.T. A discussion on a large new gold deposit found in Jiapigou gold concentrated area. *Miner. Resour. Geol.* **2003**, *17*, 683–686.
50. Zhao, Z.K.; Qi, L.J.; Chen, T. The characteristics of ore-controlling structure of Daxiangou gold deposit in Huadian area, Jilin Province. *Jilin Geol.* **2006**, *25*, 15–19.

51. Xie, H.; Shen, Y.; Jiao, X.; Meng, Q. Discussion on some important geological problems of Jiapigou gold belt, Jilin province. *Sci. Geol. Sin.* **2008**, *35*, 111–120.
52. Huang, Z.; Yuan, W.; Wang, C.; Liu, X.; Xu, X.; Yang, L. Metallogenic epoch of the Jiapigou gold belt, Jilin Province, China: Constrains from rare earth element, fluid inclusion geochemistry and geochronology. *J. Earth Syst. Sci.* **2012**, *121*, 1401–1420. [CrossRef]
53. Wilson, M. *Igneous Petrogenesis*; Unwin Hyman: London, UK, 1989.
54. Maniar, P.D.; Piccoli, P.M. Tectonic Discrimination of Granitoids. *Geol. Soc. Am. Bull.* **1989**, *101*, 635–643. [CrossRef]
55. Peccerillo, A.; Taylor, S.R. Geochemistry of Eocene calc-alkaline volcanic rocks from the Kastamonu area, Northern Turkey. *Contrib. Mineral. Petrol.* **1976**, *58*, 63–81. [CrossRef]
56. Whalen, J.B.; Currie, K.L.; Chappell, B.W. A-type granites: Geochemical characteristics, discrimination and petrogenesis. *Contrib. Mineral. Petrol.* **1987**, *95*, 407–419. [CrossRef]
57. Hoffmann, J.E.; Münker, C.; Næraa, T.; Rosing, M.T.; Herwartz, D.; Garbe-Schönberg, D.; Svahnberg, H. Mechanisms of Archean crust formation by high precision HFSE systematics on TTGs. *Geochim. Cosmochim. Acta* **2011**, *75*, 4157–4178. [CrossRef]
58. Hou, Z.H.; Wang, C.-X. Determination of 35 trace elements in geological samples by inductively coupled plasma mass spectrometry. *J. Univ. Sci. Technol. China* **2007**, *37*, 940–944.
59. Martin, H. Adakitic magmas: Modern analogues of Archaean granitoids. *Lithos* **1999**, *46*, 411–429. [CrossRef]
60. Drummond, M.S.; Defant, M.J.; Kepezhinskas, P.K. Petrogenesis of slab-derived trondhjemite- tonalite- dacite/adakite magmas. *Earth Environ. Sci. Trans. R. Soc. Edinb.* **1996**, *87*, 205–215.
61. Defant, M.; Xu, J.; Kepezhinskas, P.; Wang, Q.; Zhang, Q.; Xiao, L. Adakites: Some variations on a theme. *Acta Petrol. Sin.* **2002**, *18*, 128–142.
62. Batchelor, R.A.; Bowden, P. Petrogenetic interpretation of granitoid rock series using multicationic parameters. *Chem. Geol.* **1985**, *48*, 43–55. [CrossRef]
63. Qu, X.; Hou, Z.; Li, Y. Melt components derived from a subducted slab in late orogenic ore-bearing porphyries in the Gangdese copper belt, southern Tibetan plateau. *Lithos* **2004**, *74*, 131–148. [CrossRef]
64. Pearce, J.A.; Harris, N.B.W.; Tindle, A.G. Trace element discrimination diagrams for the tectonic interpretation of granitic rocks. *J. Petrol.* **1984**, *25*, 956–983. [CrossRef]
65. Smithies, R.H.; Champion, D.C.; Van Kranendonk, M.J. Formation of Paleoarchean continental crust through infracrustal melting of enriched basalt. *Earth Planet. Sci.Lett.* **2009**, *281*, 298–306. [CrossRef]
66. Wu, Y.; Zhou, G.; Gao, S.; Liu, X.; Qin, Z.; Wang, H.; Yang, J.; Yang, S. Petrogenesis of Neoarchean TTG rocks in the Yangtze Craton and its implication for the formation of Archean TTGs. *Precambrian Res.* **2014**, *254*, 73–86. [CrossRef]
67. Atherton, M.P.; Petford, N. Generation of sodium-rich magmas from newly underplated basaltic crust. *Nature* **1993**, *362*, 144–146. [CrossRef]
68. Windley, B.F.; Garde, A.A. Arc-generated blocks with crustal sections in the North Atlantic craton of West Greenland: Crustal growth in the Archean with modern analogues. *Earth-Sci. Rev.* **2009**, *93*, 1–30. [CrossRef]
69. Foley, S.F.; Buhre, S.; Jacob, D.E. Evolution of the Archaean crust by delamination and shallow subduction. *Nature* **2003**, *421*, 249–252. [CrossRef]
70. Geng, Y.; Du, L.; Ren, L. Growth and reworking of the early Precambrian continental crust in the North China Craton: Constraints from zircon Hf isotopes. *Gondwana Res.* **2012**, *21*, 517–529. [CrossRef]
71. Goldfarb, R.J.; Groves, D.I.; Gardoll, S. Orogenic gold and geologic time: A global synthesis. *Ore Geol. Rev.* **2001**, *18*, 1–75. [CrossRef]
72. Goldfarb, R.J.; Santosh, M. The dilemma of the Jiaodong gold deposits: Are they unique? *Geosci. Front.* **2014**, *5*, 139–153. [CrossRef]
73. Barker, F. *Trondhjemites, Dacites and Related Rocks*; Elsevier: Amsterdam, The Netherlands, 1979.
74. Foley, S.; Tiepolo, M.; Vannucci, R. Growth of early continental crust controlled by melting of amphibolite in subduction zones. *Nature* **2002**, *417*, 837–840. [CrossRef]
75. Sun, Z.; Feng, Y. Geochronology and ore-searching targets of the gold deposits in Jiapigou area, Jilin Province. *Acta Geosci. Sin.* **1997**, *18*, 367–372.
76. Sun, Z.; Feng, B.; Qing, X. The stable isotopic geology and exploration of the Jiapigou gold ore deposit, Jilin Province. *Changchun Univ. Sci. Technol.* **1998**, *28*, 142–147.
77. Zhai, M.G. Tectonic evolution and metallogenesis of North China Craton. *Miner. Depos.* **2010**, *39*, 24–36.
78. Li, B.L.; Chen, G.J.; Song, Z.W. Discussion on minerogenetic epoch of the gold deposit in Jiapigou of Jilin Province. *Glob. Geol.* **2004**, *23*, 354–359.
79. Liu, H.; Liu, J.; Sun, S.; Zhai, M. Shear-hosted mesothermal vein system in the Jiapigou goldfield, Northeast China: Implication for subsequent exploration. *Resour.Geol.* **2003**, *53*, 1–10. [CrossRef]
80. Lu, J.; Wang, N.; Xu, Z. *Early Precambrian Geology and Gold Deposits in Northern Liaoning and Southern Jili*; Jilin People's Press: Changchun, China, 1996; pp. 1–158.
81. Luo, H.; Chen, Y.; Shen, B. *The Jiapigou Gold Deposits and Ductile Shear Zone: Precambrian Ore Deposits and Structures of China*; Seismic Publishing House: Beijing, China, 1994; pp. 100–117.

82. Groves, D.I.; Goldfarb, R.J.; Gebre-Mariam, M.; Hagemann, S.G.; Robert, F. Orogenic gold deposits: A proposed classification in the context of their crustal distribution and relationship to other gold deposit types. *Ore Geol. Rev.* **1998**, *13*, 7–27. [CrossRef]
83. Groves, D.I.; Goldfarb, R.J.; Robert, F.; Hart, C.J.R. Gold deposits in metamorphic belts: Overview of current understanding, outstanding problems, future research, and exploration significance. *Econ. Geol.* **2003**, *98*, 1–29.
84. Griffin, W.L.; Begg, G.C.; O'Reilly, S.Y. Continental-root control on the genesis of magmatic ore deposits. *Nat. Geosci.* **2013**, *6*, 905–910. [CrossRef]
85. Hronsky, J.M.A.; Groves, D.I.; Loucks, R.R.; Begg, G.C. A unified model for gold mineralisation in accretionary orogens and implications for regional-scale exploration targeting methods. *Miner. Depos.* **2012**, *47*, 339–358. [CrossRef]
86. Rapp, R.P.; Shimizu, N.; Norman, M.D. Growth of early continental crust by partial melting of eclogite. *Nature* **2003**, *425*, 605–609. [CrossRef] [PubMed]
87. Said, N.; Kerrich, R.; Groves, D.I. Geochemical systematics of basalts of the lower basalt unit, 2.7 Ga Kambalda sequence: Plume impingement at a rifted craton margin. *Lithos* **2010**, *115*, 82–100. [CrossRef]
88. Moyen, J.-F.; Martin, H. Forty years of TTG research. *Lithos* **2012**, *148*, 312–336. [CrossRef]
89. Nagel, T.J.; Hoffmann, J.E.; Münker, C. Generation of Eoarchean tonalite-trondhjemite-granodiorite series from thickened mafic arc crust. *Geology* **2012**, *40*, 375–378. [CrossRef]
90. Martin, H.; Smithies, R.H.; Rapp, R.; Moyen, J.-F.; Champion, D. An overview of adakite, tonalite-trondhjemite-granodiorite (TTG), and sanukitoid: Relationships and some implications for crustal evolution. *Lithos* **2005**, *79*, 1–24. [CrossRef]
91. Martin, H.; Moyen, J.-F.; Guitreau, M.; Blichert-Toft, J.; Le Pennec, J.-L. Why Archaean TTG cannot be generated by MORB melting in subduction zones. *Lithos* **2014**, *198–199*, 1–13. [CrossRef]
92. Drummond, M.S.; Defant, M.J. A model trondhjemite-tonalite-dacite genesis and crustal growth via slab melting: Archaean to modern comparisons. *J. Geophys.Res.* **1990**, *95*, 21503–21521. [CrossRef]
93. Dai, X.; Liu, J.; Shao, J.; Jiang, R. Geology of the Jiapigou-Jinchengdong granitoid-greenstone belt, Jilin Province. *Chin. Precambrian Geol.* **1990**, *9*, 51–60.
94. Dai, J.Z.; Wang, K.Y.; Cheng, X.M. Geochemical features of ore-forming fluids in the Jiapigou gold belt, Jilin Province. *Acta Petrol. Sin.* **2007**, *23*, 2198–2206.
95. Zhai, M.; Yang, J.; Fan, H.; Miao, L.; Li, Y. A large-scale cluster of gold deposits and metallogenesis in the eastern North China craton. *Int. Geol. Rev.* **2002**, *44*, 458–476. [CrossRef]